Physica D 459 (2024) 134013

Contents lists available at ScienceDirect

Physica D

journal homepage: www.elsevier.com/locate/physd

Data-driven model identification using forcing-induced limit cycles

Dan Wilson

Department of Electrical Engineering and Computer Science, University of Tennessee, Knoxville, TN 37996, USA

ARTICLE INFO

Communicated by B. Hamzi

Keywords:
Data-driven model identification
Phase model
Phase-amplitude reduction
Model reduction
Neuroscience
Koopman analysis

ABSTRACT

This paper presents a data-driven model identification strategy that characterizes the behavior of a general dynamical system relative to a set of limit cycles that emerge in response to periodic forcing. Using time series data to infer the phase–amplitude dynamics associated with the underlying forced limit cycles, a low-order model can be obtained that accurately captures the dynamical behavior in response to arbitrary external inputs. The proposed strategy can be readily implemented in situations where full state measurements are unavailable and does not require any prior knowledge of the underlying model equations. This technique is applied to a model of coupled planar oscillators and to a model that considers the spike rate in a population of coupled conductance-based neurons where it outperforms two other commonly used data-driven model identification techniques.

1. Introduction

The equations governing the behavior of many complex, high-dimensional dynamical systems are either unknown or not well-understood. In these situations, data-driven model identification techniques can be used to obtain an accurate dynamical model that captures the salient system behaviors and accurately predicts the system response to input. Dynamic mode decomposition (DMD) is one such strategy [1–3] that is widely used due to its general applicability and relative ease of implementation. This approach provides a linear, least-squares mapping between pairs of data snapshots taken at a fixed time interval. DMD shares a close connection with Koopman analysis, which can be used to represent a general, nonlinear dynamical system as a linear, but possibly infinite dimensional operator [4–6]. This connection provides a rigorous justification for strategies such as extended DMD [7], Hankel DMD [8], and Koopman model predictive control [9], where a lifted state vector is used to obtain a better approximation for the system dynamics.

While DMD can be applied in a wide variety of situations and yields a linear model for the dynamics, it generally only considers the error between consecutive data snapshots in the fitting process. As such, its efficacy is often diminished when long-term predictions are required. Alternative strategies employ sparse fitting techniques to learn model equations by selecting a small number of terms from a large nonlinear function library to capture the relationship between snapshot pairs [10–13]. By allowing for nonlinear terms in the function library and selecting only a small subset to comprise the model dynamics, these methods mitigate the risk of overfitting and provide a model that is more interpretable in terms of the mechanisms that govern the model dynamics, especially if the function library is chosen judiciously with some knowledge of the underlying dynamical system. In a similar vein, physics-informed neural networks use machine learning techniques that explicitly account for the governing physics during training [14–16].

Rather than learning the underlying model equations that give rise to model behaviors observed in data, recent work has focused on learning representations of data relative to an underlying fixed point [17,18] or periodic orbit [19,20]. These techniques use reduced order coordinate systems that provide a universal representation of the system dynamics provided a suitable attractor can be identified. Most of these techniques leverage the isostable coordinate framework [21], which considers only the level sets of the slowest decaying eigenmodes of the Koopman operator. Other works have also considered the use of Koopman eigenfunctions to define intrinsic coordinate systems that can be used to formulate Koopman-based control problems [22]. These approaches have motivated the development of highly accurate reduced order modeling techniques that consider the dynamics in reference to a continuous family of attractors [23,24]. Of particular relevance to this work, [25] proposed a general strategy for understanding the behavior of a dynamical system by characterizing it in terms of the forced limit cycles that emerge when carefully designed periodic inputs are applied. By considering the resulting forced periodic orbits that emerge in response to the external forcing and subsequently using an adaptive phase–amplitude-based reduced order modeling approach, a low-order model can be obtained that accurately characterizes the forced dynamics in complex, high-dimensional systems. The approach from [25], however, explicitly requires knowledge of the underlying dynamical equations and requires the ability to apply input additively

E-mail address: dwilso81@utk.edu.

https://doi.org/10.1016/j.physd.2023.134013
Received 31 May 2023; Received in revised form 17 November 2023; Accepted 30 November 2023
Available online 4 December 2023

to each of the state variables; these constraints make this strategy infeasible for application in a data-driven setting.

This work extends the strategy considered in [25] by developing a purely data-driven model identification strategy that considers the dynamics in reference to a collection of periodic orbits that emerge as a result of external forcing. This model identification strategy does not require any *a priori* knowledge about the underlying system and only requires the ability to measure time-series data. In two illustrative examples, the proposed methodology yields a dynamical model that is substantially more accurate than comparable strategies that employ DMD and other isostable-coordinate-based reduction strategies. The organization of this paper is as follows: Section 2 provides necessary background information on phase and phase–amplitude reduction techniques that serve as a theoretical underpinning for the proposed model identification strategy. Section 3 gives a full description of the proposed approach and also provides a detailed list of steps required for implementation. Section 4 provides results where the proposed strategy is applied to a simple model of coupled planar oscillators as well as a more complicated model of a large population of synaptically coupled neurons. Section 5 gives concluding remarks.

2. Background

Relevant background information on phase and phase–amplitude reduction strategies for limit cycle oscillators is given below. These reduced order modeling strategies provide a theoretical underpinning for the proposed data-driven model identification strategy.

2.1. Phase reduction

Consider an ordinary differential equation of the form

$$\dot{x} = F(x,u), \tag{1}$$

where $x \in \mathbb{R}^N$ is the state, $u \in \mathbb{R}^M$ is an external input, and F sets the dynamics. Suppose that when u is held constant at $u = p$, Eq. (1) admits a stable $T(p)$-periodic orbit x_p^γ. In situations where timing of oscillations is of interest, one can define a phase $\theta \in [0, 2\pi)$ for all states $x \in x_p^\gamma$ with θ scaled so that $\frac{d\theta}{dt} = \frac{2\pi}{T(p)} = \omega(p)$ when $u = p$ is held constant. Isochrons [26,27] can be used to extend the notion of phase to the basin of attraction of the limit cycle: letting θ_1 be the phase associated with some $a \in x_p^\gamma$, the θ_1 isochron is the defined as the set of all b for which

$$\lim_{t\to 0} \|\phi(t,a) - \phi(t,b)\| = 0, \tag{2}$$

where $\phi(t,x)$ denotes the flow of (1) subject to $u = p$ and $\|\cdot\|$ can be any vector norm. Phase reduction [27–31] can be implemented by changing to variables to phase coordinates

$$\begin{aligned}\frac{d\theta}{dt} &= \frac{\partial\theta}{\partial x}\cdot\frac{dx}{dt}\\ &= \frac{\partial\theta}{\partial x}\cdot\left(F(x,p) + \frac{\partial F}{\partial u}(u-p) + O(\|u-p\|^2)\right)\\ &= \omega(p) + Z(\theta,p)(u-p) + O(\|u-p\|^2) + O(\|x - x_p^\gamma(\theta)\|^2),\end{aligned} \tag{3}$$

where $Z(\theta,p) = \frac{\partial\theta}{\partial x}^T \frac{\partial F}{\partial u}$ with all partial derivatives evaluated at $x_p^\gamma(\theta)$, the dot denotes the dot product, and ^{T} denotes the transpose. The higher order terms from Eq. (3) are typically truncated to yield a 1-dimensional reduction of the original N-dimensional ordinary differential equation that is valid in a close neighborhood of the periodic orbit.

2.2. Phase-amplitude reduction

Phase reduction of the form (3) can only be used to characterize the timing of oscillations, but can be augmented with Floquet coordinates to consider amplitude-based effects. To this end, letting $\Delta x = x - x_p^\gamma(\theta)$, to a linear approximation, $\Delta\dot{x} = J\Delta x$ where J is the Jacobian of F evaluated at $x_p^\gamma(\theta(t))$. Provided the monodromy matrix of this $T(p)$-periodic linear time varying system is diagonalizable, near x_p^γ one can employ Floquet theory [32] to write

$$x - x^\gamma(\theta) = \sum_{j=1}^{N-1} \psi_j g_j(\theta,p), \tag{4}$$

where $g_j(\theta,p)$ is a Floquet eigenfunction associated with the Floquet coordinate ψ_j. Above, the contribution from the Floquet eigenfunction g_N with Floquet multiplier $\lambda_N = 1$ has been absorbed by the phase coordinate yielding $N-1$ total Floquet coordinates. To linear order of accuracy, the Floquet coordinates can augment the phase reduction (3) to yield a set of phase–amplitude reduced equations

$$\begin{aligned}\dot{\theta} &= \omega(p) + Z(\theta,p)(u-p),\\ \dot{\psi}_j &= \kappa_j(p)\psi_j + I_j(\theta,p)(u-p),\\ j &= 1,\dots,\beta.\end{aligned} \tag{5}$$

Above, $I_j(\theta,p) = \frac{\partial\psi_j}{\partial x}^T \frac{\partial F}{\partial u}$ with all partial derivatives evaluated at $x_p^\gamma(\theta)$, and κ_j is the Floquet exponent associated with the jth Floquet eigenfunction. Additionally, in order to yield a reduced order set of equations, $N-1-\beta$ fast decaying Floquet coordinates (as gauged by the magnitude of their Floquet exponents) are ignored. Previous work [33,34] considered an extension of (5) using isostable coordinates to characterize amplitude-based effects which are valid in the basin of attraction of the limit cycle. Numerical strategies for computation of the necessary terms from (5) are discussed in [31,33].

2.3. Adaptive phase-amplitude reduction

Eqs. (3) and (5) are only valid in a close neighborhood of the limit cycle, i.e., when the Floquet coordinates are small. Consequently, they are typically only used to consider the dynamics of systems in the weakly perturbed limit. Adaptive phase–amplitude reduction [23,35] can be used to consider systems with inputs that would otherwise invalidate the weak perturbation assumption. This approach considers a family of periodic orbits to limit truncation errors associated with the phase–amplitude reduction from Eq. (5). To this end, for any $p \in P \subseteq \mathbb{R}^M$ held constant, suppose that $\dot{x} = F(x,p)$ from Eq. (1) admits a periodic orbit x_p^γ. Considering this family of periodic orbits, one can define an extended phase $\theta(x,p)$ and a set of extended Floquet coordinates $\psi_1(x,p),\dots,\psi_\beta(x,p)$. For the definition of the extended phase, the phase of each periodic orbit is unique to a constant shift; this issue can be addressed by defining a level set of the phase for each limit cycle to correspond to the crossing of some Poincaré section. For the definition of the extended Floquet coordinates, it is still assumed that the $\psi_1,\dots,\psi_\beta$ decay slowly relative to the remaining $N-1-\beta$ Floquet coordinates for all $p \in P$ as gauged by the magnitude of the associated Floquet exponents.

Intuitively, if p can be updated appropriately to limit the magnitude of the Floquet coordinates, then the associated truncation errors can be mitigated yielding a reduced order model that can accommodate large magnitude inputs. To this end, proceeding as described in [23], one can rewrite Eq. (1) according to

$$\dot{x} = F(x,p) + U_e(x,u,p), \tag{6}$$

where

$$\begin{aligned}U_e(x,u,p) &= F(x,u) - F(x,p)\\ &= \frac{\partial F}{\partial u}(u-p) + O(\|u-p\|^2),\end{aligned} \tag{7}$$

where all partial derivatives are evaluated at x and $u = p$. Considering U_e as the effective input, one can consider the system dynamics in reference to any periodic orbit x_p^γ for $p \in P$. As described in [23], allowing p to be nonstatic, transforming to phase and Floquet coordinates, and truncating higher order terms ultimately yields

$$\dot{\theta} = \omega(p) + Z(\theta,p)(u-p) + D(\theta,p)\cdot\dot{p},$$

$$\dot{\psi}_j = \kappa_j(p)\psi_j + I_j(\theta,p)(u-p) + E_j(\theta,p)\cdot\dot{p},$$
$$j = 1,\dots,\beta,$$
$$\dot{p} = G_p(p,\theta,\psi_1,\dots,\psi_\beta). \tag{8}$$

Above, $D(\theta,p)\in\mathbb{R}^M$ and $E_j(\theta,p)\in\mathbb{C}^M$ characterize how changes in the parameter set p influence θ and ψ_j, respectively, and G_p can be chosen arbitrarily to set the dynamics of p. As explained in [23], the ith element of $D(\theta,p)$ can be computed according to $-\frac{\partial x^\gamma}{\partial p_i}\cdot\frac{\partial\theta}{\partial x}$ where $\frac{\partial x^\gamma}{\partial p_i}|_{\theta_0,p} \equiv \lim_{a\to 0}(x^\gamma_{p+e_i a}(\theta_0) - x^\gamma_p(\theta_0))/a$, $\frac{\partial\theta}{\partial x}$ is evaluated in reference to x^γ_p, and e_i is the ith component of the standard unit basis. Likewise the ith element of E_j is given by $-\frac{\partial x^\gamma}{\partial p_i}\cdot\frac{\partial\psi_j}{\partial x}$ where $\frac{\partial\psi_j}{\partial x}$ is evaluated in reference to x^γ_p.

Recalling that the primary source of error in the phase–amplitude reduction from (5) results from large deviations of the state from the nominal limit cycle (and hence large values of $\psi_1,\dots,\psi_\beta$), the variable p introduced in Eq. (8) adds additional degrees of freedom with the goal of mitigating these errors by keeping the amplitude coordinates small. General heuristics for choosing G_p are discussed in [23]. Provided that each $\psi_1,\dots,\psi_\beta$ remains an order ϵ term for all time where $0<\epsilon\ll 1$, the relationship

$$x(t) = x^\gamma_p(\theta) + \sum_{j=1}^{\beta}\psi_j g_j(\theta,p) \tag{9}$$

remains accurate to leading order ϵ. The adaptive reduction (8) is used as a starting point for the proposed model identification strategy. Specific details of the proposed strategy are given in Section 3.

3. Data-driven model identification for forced nonlinear oscillations

3.1. Overview of the proposed approach

The goal of this work is to identify a reduced order, data-driven model to capture forced nonlinear oscillations in a general system of the form

$$\dot{x} = F_x(x,u),$$
$$y = C(x), \tag{10}$$

where $x\in\mathbb{R}^N$ is the state, F_x sets the dynamics of x, $u\in\mathbb{R}^M$ is an input, $y\in\mathbb{R}^K$ is the output, and C maps the state to the output. The model will be analyzed relative to an assumed stable equilibrium, x_{eq} for which $F_x(x_{\text{eq}},0)=0$. Furthermore, it will be assumed that the model displays forced oscillations resulting from at least one pair of complex-conjugate eigenvalues associated with the Jacobian evaluated at the equilibrium, however, the proposed strategy could be modified to consider situations where all eigenvalues are purely real. As distinct from standard linearization techniques, the proposed approach captures dynamics far beyond the weakly perturbed regime that would result from standard linearization of (10). Additionally, the proposed strategy is applicable even in situations where x is not observable and when both F_x and C are unknown.

The adaptive phase–amplitude reduction summarized in Section 2.3 will be used in the development of the proposed data-driven model identification technique. To this end, consider the state dynamics from (10) with the addition of an arbitrary, periodic input

$$\dot{x} = F_x\left(x, pf\left(\frac{2\pi t}{T(p)}\right) + u(t)\right). \tag{11}$$

Here, $f(\cdot)$ is assumed to be 2π-periodic in its argument ($T(p)$-periodic in time) and $p>0$ determines the magnitude of the input. The period is allowed to explicitly depend on p. Towards implementation of the adaptive phase–amplitude reduction framework described in Section 2.3, Eq. (11) will be rewritten in an autonomous form:

$$\dot{x} = F_x(x, pf(s)+u(t)),$$
$$\dot{s} = \omega(p) + f_\theta(x,s,p,u), \tag{12}$$

where $\omega = 2\pi/T$, $s\in[0,2\pi)$ is a time-like variable, and $f_\theta\in\mathbb{R}$ is an arbitrary term that can be used to modulate the time-like variable s. The exact choice of f_θ will be discussed momentarily, but note that when $f_\theta=0$, the dynamics specified by Eq. (11) are identical to those of Eq. (12). Suppose that for all allowable values of p, when taking $u(t)=0$, Eq. (11) has a stable $T(p)$-periodic orbit $x^\gamma_p(t)$ in response to the periodic forcing. Letting $X=[x^T\ s]^T$ and taking $f_\theta=0$, Eq. (12) has a corresponding periodic orbit

$$X^\gamma_p(t) = \begin{bmatrix} x^\gamma_p(t) \\ \text{mod}(\omega t, 2\pi)\end{bmatrix}. \tag{13}$$

Note that x^γ_p has the same period as the forcing. The orbit x^γ can be obtained directly in the limit that p is small provided F_x is C^∞ differentiable according to a series expansion obtained using perturbation theory. Periodic solutions typically extend beyond the small p limit and can be obtained numerically. Eq. (12) can be manipulated to be written in a similar form to (6):

$$\frac{d}{dt}\begin{bmatrix}x\\ s\end{bmatrix} = \begin{bmatrix}F_x(x,pf(s))\\ \omega(p)\end{bmatrix} + \begin{bmatrix}F_x(x,u)-F_x(x,pf(s))\\ f_\theta(x,s,p,u)\end{bmatrix}$$
$$\approx \underbrace{\begin{bmatrix}F_x(x,pf(s))\\ \omega(p)\end{bmatrix}}_{F(X,p)} + \underbrace{\begin{bmatrix}\frac{\partial F_x}{\partial u}(u-pf(s))\\ f_\theta(x,s,p,u)\end{bmatrix}}_{U_e(X,u,p)}. \tag{14}$$

Above, the first term on the right hand side of (14) sets the nominal dynamics that yield the periodic orbit from (13) and the second term acts as the effective input. Notice that the x dynamics of Eq. (14) are equivalent to those of the underlying Eq. (10) when $f_\theta=0$. Transforming to phase and Floquet coordinates applying the adaptive phase–amplitude reduction framework to (14), the phase dynamics are

$$\dot{\theta} = \omega(p) + Z_1(\theta,p)(u-pf(\theta)) + Z_2(\theta,p)f_\theta + D^T(\theta,p)\dot{p}. \tag{15}$$

Above, the terms $Z_1(\theta,p)\in\mathbb{R}^M$ and $Z_2(\theta,p)\in\mathbb{R}$ are the first M entries and last entry, respectively, of $Z(\theta,p)$, i.e., the phase response associated with the periodic orbit $X^\gamma_p(t)$. As discussed in [36], because the periodic orbit results from periodic forcing, $\theta(p,s)=\text{mod}(\theta_0+s,2\pi)$ where θ_0 is an arbitrary constant. For simplicity, one can take $\theta_0=0$ for all p so that $\theta=s$ with the phase dynamics simplifying to $\dot{\theta}=\omega(p)+f_\theta$. Applying this simplification, the adaptive phase–amplitude reduction of the form (8) becomes

$$\dot{\theta} = \omega(p) + f_\theta(p,u,\theta,\psi_1,\dots,\psi_\beta),$$
$$\dot{\psi}_j = \kappa_j(p)\psi_j + I_{j,1}(\theta,p)(u-pf(\theta)) + I_{j,2}(\theta,p)f_\theta + E_j(\theta,p)\dot{p},$$
$$j = 1,\dots,\beta,$$
$$\dot{p} = G_p(p,u,\theta,\psi_1,\dots,\psi_\beta), \tag{16}$$

where $I_{j,1}(\theta,p) = \frac{\partial\psi_j}{\partial x}^T\frac{\partial F_x}{\partial u}\in\mathbb{C}^M$ and $I_{j,2}=\frac{\partial\psi_j}{\partial s}\in\mathbb{C}$. The associated output is given by

$$y(t) = C(x(t))$$
$$= C\left(x^\gamma_p(\theta) + \sum_{j=1}^{\beta} g_j(\theta,p)\psi_j(t)\right)$$
$$\approx y^\gamma_p(\theta) + \sum_{j=1}^{\beta}\tilde{g}_j(\theta,p)\psi_j(t), \tag{17}$$

where $y^\gamma_p(\theta)\equiv C(x^\gamma_p(\theta))$ and $\tilde{g}_j(\theta,p)=\frac{\partial C}{\partial x}g_j(\theta,p)$ with partial derivatives evaluated at $x^\gamma_p(\theta)$. In the above equation, (9) is used to obtain the second line and the third line is valid first order accuracy in the Floquet coordinates. Provided G_p can be chosen so that each $\psi_1,\dots,\psi_\beta$ remain order ϵ terms for all time, the approximation (17) remains valid to leading order ϵ. Note that in Eq. (16), the terms f_θ and G_p are constrained to be functions of the state variables and input in order to yield a closed set of equations. An appropriate choice for f_θ and G_p is considered below.

As in [25], it will be assumed that κ_1 and κ_2 are complex-conjugate pairs with $\text{Real}(\kappa_1) < 0$. Such Floquet exponents generally occur when the linearized fixed point of the underlying system (10) has a complex-conjugate pair eigenvalues that can lead to a large resonant peak. In the context of the adaptive phase–amplitude reduction from (16), the focus is on keeping ψ_1 and ψ_2 small. With this goal in mind, taking

$$\begin{bmatrix} G_p \\ f_\theta \end{bmatrix} = -A_1(\theta,p)^{-1} \begin{bmatrix} \text{Real}(I_{1,1}(\theta,p))(u(t)-pf(\theta)) \\ \text{Imag}(I_{1,1}(\theta,p))(u(t)-pf(\theta)) \end{bmatrix}, \tag{18}$$

where

$$A_1(\theta,p) = \begin{bmatrix} \text{Real}(E_1(\theta,p)) & \text{Real}(I_{1,2}(\theta,p)) \\ \text{Imag}(E_1(\theta,p)) & \text{Imag}(I_{1,2}(\theta,p)) \end{bmatrix}, \tag{19}$$

the dynamics of the ψ_1 Floquet coordinate from Eq. (16) become

$$\dot{\psi}_1 = \kappa_1(p)\psi_1. \tag{20}$$

Here, $\psi_1(t)$ approaches 0 in the limit that t approaches infinity since $\text{Real}(\kappa_1) < 0$ for all $p \in P$. Of course, implementation of Eq. (18) requires that the inverse exists — this point will be discussed further in Section 3.5 for the case that $f(\theta)$ is purely sinusoidal. Provided that the inverse does exist, taking G_p and f_θ as defined in Eq. (18), ψ_1 and its complex-conjugate ψ_2 can be ignored yielding

$$\begin{aligned} \dot{\theta} &= \omega(p) + f_\theta(p,u,\theta) \\ \dot{\psi}_j &= \kappa_j(p)\psi_j + I_{j,1}(\theta,p)(u-pf(\theta)) + I_{j,2}(\theta,p)f_\theta(p,u,\theta) \\ &\quad + E_j(\theta,p)G_p(p,u,\theta), \\ &\quad j = 3,\dots,\beta, \\ \dot{p} &= G_p(p,u,\theta). \end{aligned} \tag{21}$$

Eq. (21) can be used to accurately capture large amplitude, nonlinear forced oscillations, i.e., beyond the regime for which techniques based on local linearization is valid. Intuitively, the variable θ in Eq. (21) encodes for the timing of oscillations relative to the timing on the forced periodic orbit. The variable p is an amplitude-like parameter, giving a sense of the magnitude of oscillations — larger values of p correspond to reference periodic orbits x_p^γ that are more strongly forced and hence yield larger amplitude oscillations. The isostable coordinates $\psi_3,\dots,\psi_\beta$ capture the behavior of Floquet eigenfunctions that are typically more rapidly decaying than those associated with ψ_1 and ψ_2; in practice, it is not always necessary to explicitly consider these additional isostable coordinates.

3.2. Relationship to prior work and primary contribution

Prior work [25] considered the characterization of forced, nonlinear oscillations using the adaptive phase–amplitude reduction strategy with the explicit assumption that the underlying model equations are known (so that the terms that comprise Eq. (16) can be computed numerically). Additionally, results from [25] assumed that direct input could be applied to each state variable in order to yield carefully designed periodic orbits X_p^γ. The present manuscript extends on these prior results in two important ways:

(1) This work develops and investigates purely data-driven strategies for obtaining reduced order models of the form (16) in situations where only y can be measured and where F_x is unknown.
(2) This work considers the use of general periodic inputs $u(t)$ to define the family of periodic orbits X_p^γ that consequently set the terms of the adaptive reduction from (16). This is in contrast to the carefully designed additive inputs considered in [25].

Below, Section 3.3 considers the data-driven model identification of the necessary terms of the adaptive reduction. Sections 3.4 and 3.5 consider the applicability of the proposed approach in the limit that the orbits X_p^γ are obtained using small magnitude, periodic inputs. Section 3.6 provides a list of steps for implementing the proposed approach.

3.3. Data-driven inference of the terms of the adaptive reduction

Considering the individual terms of the reduced order Eq. (16), ω is set by the external forcing, and both f_θ and G_p can be chosen arbitrarily. As such, the only unknown terms are $\kappa_j(p)$, $I_{j,1}(\theta,p)$, $I_{j,2}(\theta,p)$, and $E_j(\theta,p)$ which must be determined for $j = 1,\dots,\beta$. Once these terms have been obtained, Eq. (21) can be used to represent the behavior of the underlying model (10). A high level overview describing the necessary information required by the proposed approach is provided in Fig. 1. Specific details about the implementation of this model identification strategy are discussed in Sections 3.3.1–3.3.3 with a step-by-step description given in Section 3.6.

3.3.1. Inferring each $\kappa_j(p)$ and $I_{j,1}(\theta,p)$ from data

Consider a single periodic orbit $X_p^\gamma(t)$ that results when the input $u = pf(\omega t)$ is applied. Assume that a reasonable approximation for each $\kappa_1(p),\dots,\kappa_\beta(p)$ is already known, for instance, using the relation (B.4) which is valid in the limit that p is small or with knowledge of $\kappa_1(p-\Delta p),\dots,\kappa_\beta(p-\Delta p)$, i.e., that has already been obtained from a nearby input induced orbit. For the moment, suppose that $f_\theta = 0$ so that $\theta = \omega t$. Additionally taking $G_p = 0$, i.e., so that $\dot{p} = 0$, the reduced order equations for the dynamics of the Floquet coordinates from (21) simplify to

$$\dot{\psi}_j = \kappa_j(p)\psi_j + I_{j,1}(\omega t,p)(u-pf(\omega t)), \tag{22}$$

for $j = 1,\dots,\beta$. Applying an input $u(t) = pf(\omega t) + e_i\alpha(t)$ where $\alpha(t)$ is a small, arbitrary signal and e_i is an appropriately sized element of the standard unit basis, Eq. (22) becomes

$$\dot{\psi}_j = \kappa_j(p)\psi_j + I^i_{j,1}(\omega t,p)\alpha(t), \tag{23}$$

where the term $I^i_{j,1}$ denotes the ith element of $I_{j,1}$. An explicit solution to (23) can be obtained using the variation of constants formula [37],

$$\psi_j(t) = \psi(t_0)\exp(\kappa_j(t-t_0)) + \int_{t_0}^{t} \exp(\kappa_j(t-s))I^i_{j,1}(\omega s)\alpha(s)ds. \tag{24}$$

According to Eq. (24), provided t is sufficiently larger than t_0 so that the influence of the initial condition is forgotten, $\psi_j(t)$ is directly recoverable given knowledge of $I^i_{j,1}(\omega t)$. Next considering the output equation from (17), for t large enough one finds

$$y(t) - y_p^\gamma(t) = \int_{t_0}^{t} \left(\sum_{j=1}^{\beta} \tilde{g}_j(\omega t,p)\exp(\kappa_j(t-s))I^i_{j,1}(\omega s)\alpha(s) \right) ds. \tag{25}$$

Recalling that $\tilde{g}_j(\theta,p) = \frac{\partial C}{\partial x} g_j(\theta,p)$ where $g_j(\theta,p)$ is a Floquet eigenfunction, it is possible to scale each $\tilde{g}_j(\theta,p)$ so that $e_m^T\tilde{g}_j(0,p) = 1$ provided that $e_m^T\tilde{g}_j(0,p) \neq 0$. Here, e_m is an arbitrary element of the standard unit basis. Using such a scaling, multiplying Eq. (25) by e_m^T on both sides yields

$$e_m^T(y(\sigma T) - y_p^\gamma(\sigma T)) = \int_{t_0}^{\sigma T} \left(\sum_{j=1}^{\beta} \exp(\kappa_j(\sigma T - s))I^i_{j,1}(\omega s)\alpha(s) \right) ds. \tag{26}$$

Above, σ must be an integer chosen large enough so that the initial conditions are forgotten and T is the period of the applied input (note here that $\theta = 0$ when $t = \sigma T$). Recalling that each $I^i_{j,1}(\theta)$ is 2π-periodic, one can represent each $I^i_{j,1}(\omega s)$ from Eq. (26) with a Fourier series

$$I^i_{j,1}(\omega s) = b_0^{j,1,i} + \sum_{k=1}^{\mu} a_k^{j,1,i}\sin(k\omega s) + b_k^{j,1,i}\cos(k\omega s), \tag{27}$$

where μ sets the number of terms of the Fourier series that are retained. Noticing that the coefficients of the Fourier series expansion do not depend on s, they can be pulled out of the integral from Eq. (26) to yield

$$e_m^T(y(\sigma T) - y_p^\gamma(\sigma T)) = \Gamma^T(\sigma T)Y, \tag{28}$$

where $Y \in \mathbb{C}^{\beta(2\mu+1)}$ is a vector containing the nontruncated Fourier series coefficients of each $I^i_{1,1}(\omega s),\dots,I^i_{\beta,1}(\omega s)$ and $\Gamma \in \mathbb{C}^{\beta(2\mu+1)}$ is

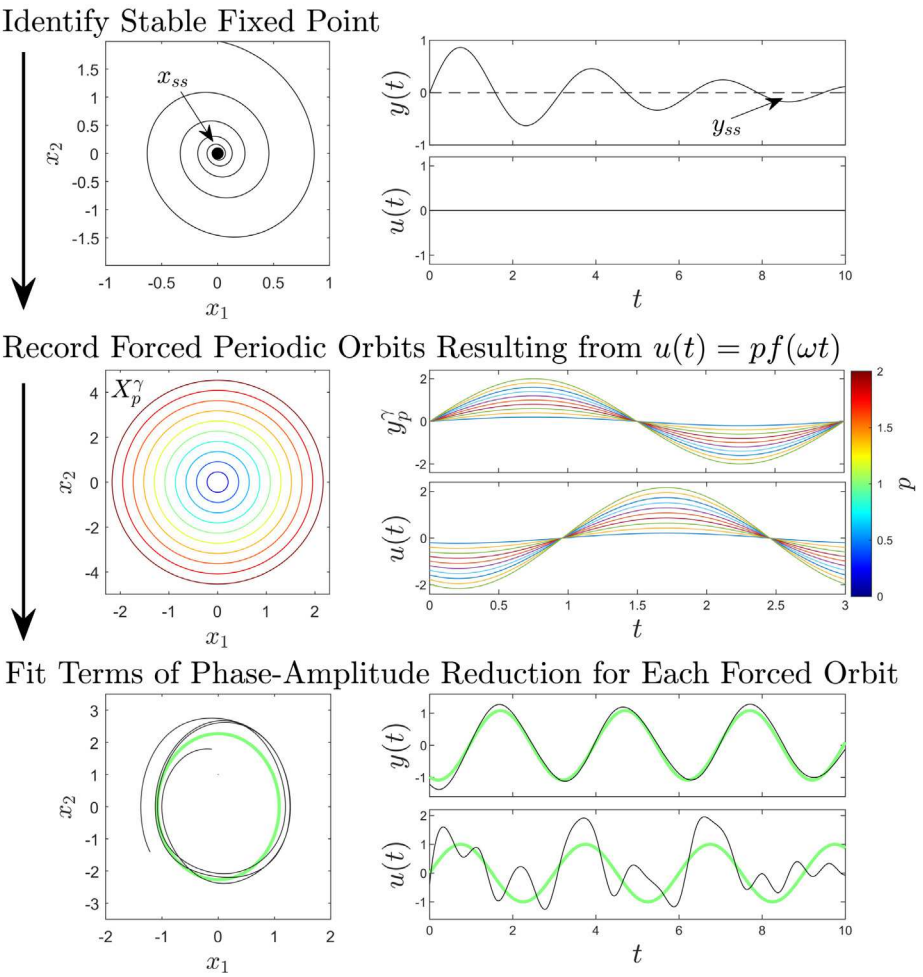

Fig. 1. The figure above represents a high level overview of the necessary information required by the proposed model identification strategy for a general dynamical system. (Top panels) In the absence of input, the model identification strategy requires a stable fixed point x_{ss}; the corresponding model output approaches the constant y_{ss} in the absence of external forcing. (Middle panels) Forced limit cycles X_p^γ emerge in response to the periodic forcing $u(t) = pf(\omega t)$; the corresponding steady state output y_p^γ is recorded. The colors here represent different periodic orbits and associated periodic inputs for different values of p. (Bottom panels) For each forced limit cycle, additional perturbations are applied and the resulting output $y(t)$ is compared to y_p^γ to infer the terms of the phase-isostable reduction of the form (16) yielding a low-order model. Here for instance, inputs and outputs are considered relative to the $p = 1$ periodic orbit.

comprised of the remaining terms and is arranged so that Eq. (28) is identical to Eq. (26). Note that the computation of the terms that comprise Γ requires knowledge of each $\kappa_1, \dots, \kappa_\beta$ (which are known to a good approximation) and $\alpha(t)$ (the input applied to the system). As such all terms of $\Gamma(\sigma T)$ can be computed leaving Y as the only unknowns. With enough measurements, one can ultimately obtain a least-squares estimate of Y according to

$$Y = \begin{bmatrix} \Gamma^T(\sigma T) \\ \Gamma^T((\sigma+1)T) \\ \vdots \\ \Gamma^T((\sigma+n)T) \end{bmatrix}^\dagger \begin{bmatrix} e_m^T(y(\sigma T) - y_p^\gamma(\sigma T)) \\ e_m^T(y((\sigma+1)T) - y_p^\gamma((\sigma+1)T)) \\ \vdots \\ e_m^T(y((\sigma+n)T) - y_p^\gamma((\sigma+n)T)) \end{bmatrix}, \tag{29}$$

where n corresponds to the number of periods the stimulus $u(t)$ is applied after the influence of initial conditions has been forgotten and † is the pseudoinverse. Once an estimate for Y has been obtained, refined estimates for $K = \begin{bmatrix} \kappa_1 & \dots & \kappa_\beta \end{bmatrix}^T$ can be obtained using a Newton iteration. To this end, defining

$$E(K) = \begin{bmatrix} \Gamma^T(\sigma T) \\ \Gamma^T((\sigma+1)T) \\ \vdots \\ \Gamma^T((\sigma+n)T) \end{bmatrix} Y - \begin{bmatrix} e_m^T(y(\sigma T) - y_p^\gamma(\sigma T)) \\ e_m^T(y((\sigma+1)T) - y_p^\gamma((\sigma+1)T)) \\ \vdots \\ e_m^T(y((\sigma+n)T) - y_p^\gamma((\sigma+n)T)) \end{bmatrix} \tag{30}$$

as the error associated with the estimate from Eq. (29), a Newton iteration can be performed to update the estimate of the Floquet exponents by solving

$$\begin{aligned} 0 &= E(K + \Delta K) \\ &\approx E(K) + \frac{\partial E}{\partial K}\Delta K, \end{aligned} \tag{31}$$

where ΔK is a small refinement to the Floquet exponents. A least squares solution for Eq. (31) can be obtained according to

$$\Delta K = -\frac{\partial E}{\partial K}^\dagger E(K). \tag{32}$$

Above, the elements of $\partial E/\partial K$ can be estimated via numerical differentiation. For instance, by changing the value of κ_1 to $\kappa_1 + \epsilon$ for some small value of ϵ, reevaluating Y after the shift in the Floquet exponent,

and subsequently computing $E(K + e_1\epsilon)$, the first column of $\partial E/\partial K$ can be approximated according to $(E(K + e_1\epsilon) - E(K))/\epsilon$. Refinements can be implemented iteratively by computing ΔK multiple times until convergence. Recall that strategy described above only yields estimates of the ith element of each $I_{1,1}(\theta), \dots, I_{\beta,1}(\theta)$ by applying inputs of the form $u(t) = pf(\omega t) + e_i\alpha(t)$. The remaining elements can be repeated by applying additional inputs $u(t) = pf(\omega t) + e_i\alpha(t)$ for $i = 1, \dots, M$ and estimating the associated terms according to Eq. (29).

3.3.2. Inferring each $I_{j,2}(\theta, p)$ from data

Consider a single periodic orbit $X_p^\gamma(t)$ that results when the input $u = pf(\omega t)$ is applied. Assume that an approximation for each $\kappa_1(p), \dots, \kappa_\beta(p)$ has already been obtained using the strategy described in Section 3.3.1. Let $u(t) = pf(\theta)$, this time removing the requirement that $f_\theta(t) = 0$ for all t. Also, take $G_p = 0$ so that $\dot{p} = 0$. In this case, the reduced order equations for the dynamics of the phase and Floquet coordinates from (21) simplify to

$$\begin{aligned} \dot{\theta} &= \omega(p) + f_\theta(t), \\ \dot{\psi}_j &= \kappa_j(p)\psi_j + I_{j,2}(\theta, p) f_\theta(t), \end{aligned} \tag{33}$$

for $j = 1, \dots, \beta$. The phase dynamics are obtained according to

$$\theta(t) = \operatorname{mod}\left(\theta_0 + \int_0^t \big(\omega + f_\theta(t)\big)dt, 2\pi\right) \equiv \hat{\theta}(t), \tag{34}$$

where θ_0 is the initial condition and is taken to be zero for convenience. Notice that the Floquet coordinate dynamics of (33) are similar to those from (23) with $f_\theta(t)$ taking the place of $\alpha(t)$. Repeating the analysis that starts with Eq. (23) and culminates in Eq. (25), one finds

$$y(t) - y_p^\gamma(t) = \int_{t_0}^t \left(\sum_{j=1}^\beta \tilde{g}_j(\hat{\theta}(s), p) \exp(\kappa_j(t-s)) I_{j,2}(\hat{\theta}(s)) f_\theta(s)\right) ds, \tag{35}$$

for any t large enough for the influence of initial conditions to be forgotten. With the same scaling on each $\tilde{g}_j(\theta, p)$ described under Eq. (25) it will once again be assumed that $e_m^T \tilde{g}_j(0, p) = 1$. With this in mind, letting t_k^* correspond to the kth time that $\hat{\theta}$ crosses 0, multiplying Eq. (35) on both sides by e_m^T admits the simplification

$$e_m^T(y(t_k^*) - y_p^\gamma(t_k^*)) = \int_{t_0}^{t_k^*} \left(\sum_{j=1}^\beta \exp(\kappa_j(t_k^* - s)) I_{j,2}(\hat{\theta}(s)) f_\theta(s)\right) ds, \tag{36}$$

for any t_k^* large enough so that the influence from initial conditions is forgotten. $I_{j,2}(\theta)$ for $j = 1, \dots, \beta$ are the only unknown term in the above equation. As before, representing these 2π-periodic functions using a truncated Fourier series

$$I_{j,2}(\theta) = b_0^{j,2} + \sum_{k=1}^\mu a_k^{j,2} \sin(k\theta) + b_k^{j,2} \cos(k\theta), \tag{37}$$

the Fourier coefficients can be pulled out of the integral from (36) allowing it to be written as

$$e_m^T(y(t_k^*) - y_p^\gamma(t_k^*)) = \Gamma^T(t_k^*) Y, \tag{38}$$

where $Y \in \mathbb{C}^{\beta(2\mu+1)}$ is a vector containing the Fourier series coefficients of each $I_{1,2}(\theta), \dots, I_{\beta,2}(\theta)$ and $\Gamma \in \mathbb{C}^{\beta(2\mu+1)}$ is comprised of the remaining terms. Similar to Eq. (29), one can use (38) to obtain a least-squares estimate for the unknown Fourier coefficients

$$Y = \begin{bmatrix} \Gamma^T(t_k^*) \\ \Gamma^T(t_{k+1}^*) \\ \vdots \\ \Gamma^T(t_{k+n}^*) \end{bmatrix}^\dagger \begin{bmatrix} e_m^T(y(t_k^*) - y_p^\gamma(t_k^*)) \\ e_m^T(y(t_{k+1}^*) - y_p^\gamma(t_{k+1}^*)) \\ \vdots \\ e_m^T(y(t_{k+n}^*) - y_p^\gamma(t_{k+n}^*)) \end{bmatrix}, \tag{39}$$

where n corresponds to the number of crossings of $\hat{\theta} = 0$ that are used in the fitting.

3.3.3. Inferring each $E_j(\theta, p)$ from data

Ref. [19] established direct relationships between the gradients of the Floquet coordinates and the associated terms $E_j(\theta, p)$. Of particular use here, let $\zeta_j(\theta, p) \equiv \frac{\partial \psi_j}{\partial X}^T \frac{\partial F}{\partial p} \in \mathbb{C}^1$ where all partial derivatives are evaluated on the periodic orbit X_p^γ. Note that while $\zeta_j(\theta, p)$ is similar to $I_j(\theta, p)$ as defined below Eq. (5), these two terms are not identical. As illustrated in Section 3.2 of [19] $E_j(\theta, p)$ is directly related to $\zeta_j(\theta, p)$ according to

$$\begin{aligned} E_j(\theta, p) = \frac{b_0^j}{\kappa_j} + \sum_{m=1}^\infty \Bigg[&\frac{a_m^j \kappa_j \sin(m\theta)}{\kappa_j^2 + \omega^2 m^2} + \frac{a_m^j m\omega \cos(m\theta)}{\kappa_j^2 + \omega^2 m^2} \\ &- \frac{b_m^j m\omega \sin(m\theta)}{\kappa_j^2 + \omega^2 m^2} + \frac{b_m^j \kappa_j \cos(m\theta)}{\kappa_j^2 + \omega^2 m^2} \Bigg], \end{aligned} \tag{40}$$

where a_k^j and b_k^j are Fourier coefficients of $\zeta_j(\theta, p)$, i.e.,

$$\zeta_j(\theta, p) = b_0^j + \sum_{m=1}^\infty \left[a_m^j \sin(m\theta) + b_m^j \cos(m\theta)\right]. \tag{41}$$

Ultimately, the relation (40) allows for the inference of each $E_j(\theta, p)$ for $j = 1, \dots, \beta$ without the need for additional data beyond what is required to implement the strategies from Sections 3.3.1 and 3.3.2. Indeed, considering the specific model (12) used here

$$\begin{aligned} \zeta_j(\theta, p) &= \frac{\partial \psi_j}{\partial X}^T \frac{\partial F}{\partial p} \\ &= \begin{bmatrix} \frac{\partial \psi_j}{\partial x}^T & \frac{\partial \psi_j}{\partial s} \end{bmatrix} \begin{bmatrix} \frac{\partial F_x}{\partial u} f(\theta) \\ \frac{\partial \omega}{\partial p} \end{bmatrix} \\ &= I_{j,1}(\theta, p) f(\theta) + I_{j,2}(\theta, p) \frac{\partial \omega}{\partial p}. \end{aligned} \tag{42}$$

Supposing that $I_{j,1}(\theta, p)$ and $I_{j,2}(\theta, p)$ have already been obtained using the strategy described in Sections 3.3.1 and 3.3.2, respectively, $\zeta_j(\theta, p)$ can be computed according to (42) and subsequently used to infer $E_j(\theta, p)$ according to Eq. (40).

3.4. Terms of the adaptive reduction in the limit of weak forcing

Here, the terms of the adaptive reduction are considered for periodic orbits of (12) that are valid in the weakly perturbed limit, i.e., using small values of p to yield the resulting periodic orbit. To begin, consider the underlying system (10) using the T-periodic input $u(t) = pf(\omega t)$ where $\omega = 2\pi/T$. Also suppose that $p = O(\epsilon)$ where $0 < \epsilon \ll 1$ so that local linearization techniques are applicable. For simplicity of exposition, assume that $x_{\text{eq}} = 0$. To linear order, the state dynamics of Eq. (10) becomes

$$\dot{x} = Ax + Bpf(\omega t), \tag{43}$$

where $A = \frac{\partial F_x}{\partial x}$ and $B = \frac{\partial F_x}{\partial u}$, both evaluated at the stable fixed point. The variation of constants formula [37] can be used to write the state as a function of time

$$x(t) = e^{A(t-t_0)} x(t_0) + \int_{t_0}^t e^{A(t-\tau)} Bpf(\omega\tau) d\tau, \tag{44}$$

where e^A denotes the matrix exponential of A and t_0 is the initial time. In the limit that t approaches infinity, Eq. (44) approaches a forced periodic orbit given by

$$x_p^\gamma(t) = p\left(e^{At} x_0 + \int_0^t e^{A(t-\tau)} Bf(\omega\tau) d\tau\right), \tag{45}$$

where

$$x_0 = \left[\text{Id} - e^{AT}\right]^{-1} \int_0^T e^{A(t-\tau)} Bf(\omega\tau) d\tau, \tag{46}$$

with Id being an appropriately sized identity matrix. Note that the inverse in Eq. (46) is guaranteed to exist because A is a stable matrix

so that the eigenvalues of e^{AT} have magnitude less than 1. With this in mind, to leading order, the measured periodic orbit is

$$y_p^\gamma(t) = \frac{\partial C}{\partial x} x_p^\gamma(t). \tag{47}$$

Towards computation of the terms of the adaptive phase–amplitude reduction from Eq. (16), once again considering the autonomous form of the ordinary differential equation with state $X = \begin{bmatrix} x^T & s \end{bmatrix}^T$, the corresponding periodic orbit of (12), $X_p^\gamma(t)$, is given by Eq. (13). Turning attention towards the Floquet exponents and gradients of the Floquet coordinates, the Jacobian evaluated on this periodic orbit can be written as

$$J(t) = \begin{bmatrix} A & 0 \\ 0 & 0 \end{bmatrix} + O(\epsilon). \tag{48}$$

To obtain the above equation, recall that $p = O(\epsilon)$; consequently from Eq. (45), $x_p^\gamma(t) = O(\epsilon)$ so that $\frac{\partial F_x}{\partial x} = A + O(\epsilon)$. To leading order ϵ, solutions nearby X_p^γ evolve according to

$$\Delta \dot{X} = \begin{bmatrix} A & 0 \\ 0 & 0 \end{bmatrix} \Delta X + O(\epsilon), \tag{49}$$

where $\Delta X = X - X_p^\gamma$. While Eq. (49) is linear time varying (owing to the $O(\epsilon)$ terms), it is linear time invariant to leading order. Considering (49), Appendix B provides approximations for $\frac{\partial \psi_j}{\partial X}$ in Eq. (B.10). This approximation can be used to determine $I_{j,1}$ and $I_{j,2}$ to leading order. In particular

$$\begin{aligned} I_{j,1}(\theta, p) &= \left(\frac{\partial \psi_j}{\partial x}\right)^T \frac{\partial F_x}{\partial u} \\ &= w_j^T B \exp(-\theta i m). \end{aligned} \tag{50}$$

where (w_j, λ_j) is a left eigenvector/eigenvalue pair of A associated with the jth Floquet exponent. Above, the first line comes from the definition given after Eq. (16) and the second line is obtained by substituting the first N elements of $\frac{\partial \psi_j}{\partial X}$ and using the coordinate transformation $\theta = \omega t$. Additionally,

$$\begin{aligned} I_{j,2}(\theta, p) &= \frac{\partial \psi_j}{\partial s} \\ &= p \eta_j(\theta/\omega), \end{aligned} \tag{51}$$

where the first line comes from the definition given after Eq. (16) and the second line is obtained by substituting (B.12) keeping in mind that $b_{j,2}$ from (B.12) is identical to $\partial \psi_1 / \partial s$ and using the coordinate transformation $\theta = \omega t$. Considering the above analysis, both y_p^γ from (47) and $I_{j,2}$ from (51) are proportional to p (to leading order) in the limit of small forcing. Conversely, $I_{j,1}$ from Eq. (50) does not depend on p. Likewise from (B.4), to leading order the Floquet exponent κ_j depends directly on the period of forcing and the corresponding eigenvalues of A denoted by λ_j.

3.5. Implementation using purely sinusoidal forcing

In order to implement Eq. (21), the matrix inverse from Eq. (18) used to determine the terms G_p and f_θ must exist. Here, letting $L \in \mathbb{R}^M$ it is shown that when taking $pf(2\pi t/T) = pL \sin(2\pi t/T)$ to yield the periodic orbits that comprise the adaptive phase–amplitude reduction from (16), provided the periodic input excites the mode associated with the ψ_1 Floquet coordinate, the transformation to (21) is always possible in the limit that p is small.

To this end, consider the underlying system (10) taking $u(t) = pL \sin(\omega t)$ where $\omega = 2\pi/T$. When p is small, the linearized dynamics are identical to those from (43). Let λ_1 and λ_2 be a simple, complex-conjugate pair of eigenvalues of A that give rise to resonant oscillations with $\mathrm{Imag}(\lambda_1) > 0$. It is assumed that $w_1^T BL \neq 0$ where w_1 is the left eigenvector associated with the λ_1 eigenvalue; this ensures that the input excites the mode associated with λ_1. To proceed, let $D = Q^{-1}AQ$ be the Jordan normal form of A where Q is an appropriately defined invertible matrix. Considering the linearized dynamics (43) with a change of variables $x_J = Q^{-1}x$ yields dynamics

$$\dot{x}_J = Dx_J + Q^{-1}BLp \sin(\omega t). \tag{52}$$

Because λ_1 is simple, it will have a Jordan block of size 1 with eigenvalue λ_1. Letting $(e_k^T D)_k = \lambda_1$ where e_i is the ith element of the standard unit basis, one can write

$$\dot{x}_J^k = \lambda_1 x_J^k + p\delta \sin(\omega t), \tag{53}$$

where x_J^i denotes the ith element of x_J. Notice that $\delta = e_k^T Q^{-1} BL = w_1^T BL \neq 0$. In response to sinusoidal forcing, Eq. (53) has a stable steady state response

$$x_{J,ss}^k(t) = -\frac{p\delta}{\omega^2 + \lambda_1^2}(\lambda_1 \sin(\omega t) + \omega \cos(\omega t)). \tag{54}$$

Transforming back to the original coordinates taking $x = Qx_J$, the stable forced periodic orbit $x_p^\gamma(t)$ can be written as

$$\begin{aligned} x_p^\gamma(t) &= x_{J,ss}^k(t) q_k + \sum_{j \neq k} x_{J,ss}^j(t) q_j \\ &= -\frac{p\delta}{\omega^2 + \lambda_1^2}(\lambda_1 \sin(\omega t) + \omega \cos(\omega t)) q_k + \sum_{j \neq k} x_{J,ss}^j(t) q_j, \end{aligned} \tag{55}$$

where q_j is the jth column of Q.

Ultimately, the goal here is to show that the matrix inverse from Eq. (18) exists when p is small. To do so, it is necessary to consider $E_1(\theta, p)$ and $I_{1,2}(\theta, p)$ as defined below Eqs. (8) and (16), respectively. Towards this goal, recalling that $I_{1,2}(\theta, p) = \frac{\partial \psi_1}{\partial s}$ and considering Eq. (A.5) which is valid in the limit that p is small,

$$\begin{aligned} 0 &= \left(\frac{\partial \psi_1}{\partial X}\right)^T \frac{dX_p^\gamma}{dt} \\ &= \begin{bmatrix} w_1^T \exp(-\omega i m t) & \frac{\partial \psi_1}{\partial s} \end{bmatrix} \\ &\quad \times \begin{bmatrix} -\frac{p\delta\omega}{\omega^2 + \lambda_1^2}(\lambda_1 \cos(\omega t) - \omega \sin(\omega t)) q_k + \sum_{j \neq k} \frac{d}{dt}\left(x_{J,ss}^j(t)\right) q_j \\ \omega \end{bmatrix}, \end{aligned} \tag{56}$$

where the second line is obtained by substituting (B.10) for $\partial \psi_1 / \partial X$ (noting that $b_{j,2}$ from (B.10) is identical to $\partial \psi_1 / \partial s$), recalling that $X_p^\gamma = [x_p^{\gamma T} \bmod(\omega t, 2\pi)]^T$, and substituting Eq. (55) for x_p^γ. Recalling that λ_1 is a simple eigenvalue, v_1 (the eigenvector associated with λ_1) is identical to q_k and the corresponding left eigenvector w_1 is orthogonal to q_j for $j \neq k$. With this in mind, Eq. (56) simplifies to

$$\begin{aligned} \frac{\partial \psi_1}{\partial s} &= \frac{p\delta}{\omega^2 + \lambda_1^2} \exp(-\omega i m t)(\lambda_1 \cos(\omega t) - \omega \sin(\omega t)) \\ &= \frac{p\delta}{\omega^2 + \lambda_1^2}(\cos(m\omega t) - i \sin(m\omega t))(\lambda_1 \cos(\omega t) - \omega \sin(\omega t)). \end{aligned} \tag{57}$$

With the coordinate transformation $\theta = \omega t$ and recalling from the definition given after Eq. (16) that $\frac{\partial \psi_1}{\partial s} = I_{1,2}$, one finds

$$I_{1,2}(\theta, p) = \frac{p\delta}{\omega^2 + \lambda_1^2}(\cos(m\theta) - i \sin(m\theta))(\lambda_1 \cos(\theta) - \omega \sin(\theta)). \tag{58}$$

Next, focusing attention on $E_1(\theta, p)$, per the definition given under Eq. (8)

$$\begin{aligned} E_1(\theta(t), p) &= -\left(\frac{\partial \psi_1}{\partial X}\right)^T \frac{\partial X^\gamma}{\partial p} \\ &= -\begin{bmatrix} w_1^T \exp(-\omega i m t) & \frac{\partial \psi_1}{\partial s} \end{bmatrix} \\ &\quad \times \begin{bmatrix} -\frac{\delta}{\omega^2 + \lambda_1^2}(\lambda_1 \sin(\omega t) + \omega \cos(\omega t)) q_k + \sum_{j \neq k} \frac{\partial}{\partial p}\left(x_{J,ss}^j(t)\right) q_j \\ 0 \end{bmatrix} \\ &= \frac{\delta}{\omega^2 + \lambda_1^2} \exp(-\omega i m t)(\lambda_1 \sin(\omega t) + \omega \cos(\omega t)). \end{aligned} \tag{59}$$

Above, the second line is obtained by substituting (B.10) for $\partial \psi_1 / \partial X$, recalling that $X_p^\gamma = [x_p^{\gamma T} \bmod(\omega t, 2\pi)]^T$, and substituting Eq. (55) for x_p^γ.

The third line is obtained by exploiting the relationships between ω_1 and q_j as described below Eq. (56). With the coordinate transformation $\theta = \omega t$, Eq. (59) simplifies to

$$E_1(\theta, p) = \frac{\delta}{\omega^2 + \lambda_1^2}(\cos(m\theta) - i\sin(m\theta))(\lambda_1 \sin(\theta) + \omega\cos(\theta)). \tag{60}$$

Finally, considering both $I_{1,2}(\theta, p)$ and $E_1(\theta, p)$ from Eqs. (58) and (60), the determinant of $A_1(\theta, p)$ from Eq. (19) simplifies to

$$\det(A_1(\theta, p)) = \frac{\mathrm{Im}(\lambda_1)\omega p|\delta|^2}{|\omega^2 + \lambda_1^2|^2}, \tag{61}$$

where $|a|$ denotes the magnitude of $a \in \mathbb{C}$. In particular, $\det(A_1(\theta, p)) \neq 0$. As such, $A_1(\theta, p)^{-1}$ always exists allowing for the implementation of Eq. (21). Note that this conclusion is only valid in the limit that p is small, i.e., in the linear regime. Nonetheless, as seen in the examples from Section 4, Eq. (21) can typically be used to implement the proposed approach far beyond the linear regime to yield a low-dimensional model that accurately captures the response to general inputs.

3.6. List of steps required to implement the proposed model identification strategy

The proposed model identification strategy discussed in Sections 3.1–3.3 can be implemented using the steps summarized below. Implementation of this strategy yields a low order model of the form (21) that can be used to the general input–output dynamics in a general model of the form (10).

(1) Identify a fixed point of the model (10) for which $F_x(x_{ss}, 0) = 0$ with steady state output $y_{ss} = C(x_{ss})$. The linearized version of (10) is assumed to have a complex-conjugate pair of eigenvalues $\lambda_{1,2} = \mathrm{Real}(\lambda_1) \pm i\mathrm{Imag}(\lambda_1)$ that give rise to resonant oscillations. A coarse estimate of these eigenvalues can be obtained, for instance, by identifying the resonant frequency and observing the associated decay of oscillations back to the fixed point. Determine how many (if any) additional Floquet coordinates to include in the fitting; Floquet coordinates $\psi_3, \ldots, \psi_\beta$ can be used to capture the behavior of additional eigenmodes that have relatively small contributions to the dynamics.

(2) Define a periodic input $u(t) = pf(\omega t)$ which will be used to determine periodic orbits X_p^γ.

(3) Initially taking $p = p_0$ to be small enough so that the system can be well approximated by local linearization, record the output $y_{p_0}^\gamma$ associated with the resulting periodic orbit.

(4) For $i = 1, \ldots, m$, apply an input $u(t) = p_0 f(\omega t) + e_i\alpha(t)$ to (10) where $\alpha(t)$ as defined below Eq. (22) and e_i is the ith element of the standard unit basis. Record the output $y(t)$. Use Eq. (29) to estimate the Fourier series coefficients of $I_{1,1}^k(\theta, p_0), \ldots, I_{\beta,1}^k(\theta, p_0)$ for some arbitrary choice of $k \in \{1, \ldots, m\}$. Subsequently update the estimate for the Floquet exponents by applying Eq. (32) and iterate until the estimate for the Floquet exponents converges. For the remaining $i \neq k$, use Eq. (29) to estimate the Fourier series coefficients of $I_{1,1}^i(\theta, p_0), \ldots, I_{\beta,1}^i(\theta, p_0)$.

(5) Let $\hat{\theta}(t) = \mathrm{mod}(\int_0^t (\omega + f_\theta(t))dt, 2\pi)$ as defined in Eq. (34) for some prespecified $f_\theta(t)$. Apply the input $u(t) = p_0 f(\hat{\theta})$ and record the output $y(t)$. Use this information to estimate the Fourier series coefficients of $I_{1,2}(\theta, p_0), \ldots, I_{\beta,2}(\theta, p_0)$ according to Eq. (39).

(6) Use Eq. (40) to compute the terms of each $E_j(\theta, p_0)$ for $j = 1, \ldots, \beta$. The terms of the right hand side of (40) can be computed using Eqs. (41) and (42) which in turn use information that is obtained in Steps 4 and 5.

Steps 3 through 5 must be repeated taking $p = p_0 + i\Delta p$ for $i = 1, 2, \ldots$. As part of Step 4, an initial guess for $\kappa_j(p_0 + i\Delta p)$ can be taken as $\kappa_j(p_0 + (i-1)\Delta p)$, i.e., the Floquet exponent inferred for the prior orbit.

Upon completion of Steps 1–6 for each p-limit cycle, $I_{j,1}(\theta, p)$, $I_{j,2}(\theta, p)$, $E_j(\theta, p)$ and $\kappa_j(p)$ for $j = 1, \ldots, \beta$ can be computed for any p in the allowable range using linear interpolation. The terms f_θ and G_p in the implementation of the reduced order model can be computed according to (18). In response to an arbitrary input $u(t)$, provided the Floquet coordinates $\psi_3, \ldots, \psi_\beta$ remain $O(\epsilon)$ terms, the approximation for the output $y(t) \approx y_p^\gamma(\theta(t))$ is accurate to leading order ϵ.

A few general notes about the implementation of the proposed model identification strategy are highlighted below:

Note (1) In practice, it often works well to take $\omega(p)$ near, but not identical to the resonant frequency associated with the ψ_1 Floquet coordinate. As discussed in [25], in the limit that p is small and the frequency is exactly identical to the resonant frequency (i.e., when $\omega = \mathrm{Imag}(\lambda_1)$, the Floquet exponent κ_1 becomes identical to κ_2, thereby precluding implementation of the reduced order modeling strategy. As p increases, the resonant frequency may drift making it necessary to update $\omega(p)$. In simulations considered here, it worked well to target $\mathrm{Imag}(\kappa_1) \approx \pi/2$, increasing or decreasing $\omega(p)$ as necessary in order to achieve this target.

Note (1) If $f(\omega t) = \sin(\omega t)$ is used to define the periodic orbits X_p^γ, when both p is small and ω is chosen to be close to the natural frequency so that $m = 1$, all Fourier modes of $I_{1,2}(\theta, p)$ are zero beyond second order in the Fourier series, as can be inferred from Eq. (58). It is straightforward to show that this property holds for all $I_{1,2}(\theta, p), \ldots, I_{\beta,2}(\theta, p)$. Coupled with the fact that the Fourier series coefficients for each $I_{j,1}(\theta, p)$ are zero beyond first order, the Fourier series basis from (27) and (37) only requires $\mu = 1$ and $\mu = 2$, respectively, when p is small. In practice, even when p is larger it is often useful to take μ to be small to mitigate the risk of overfitting.

Note (1) When noise is present in the system, $\alpha(t)$ and f_θ from Steps 4 and 5 must be large enough to obtain a strong signal relative to the noise strength but must be small enough so that the inputs do not drive the system too far from the underlying limit cycle. In numerical results presented below, it often worked well to use a continuous signal for $\alpha(t)$ and to use a series of short pulses for $f_\theta(t)$.

4. Results

4.1. Coupled planar oscillators

As a preliminary example, the proposed model identification strategy is applied to a population of $N = 10$ heterogeneous planar oscillators:

$$\begin{aligned}\dot{a}_j &= \sigma a_j(\mu_j - r_j^2) - b_j(1 + \rho_j(r_j^2 - \mu_j)) + \frac{K}{N}\sum_{j\neq i} a_j + u(t),\\ \dot{b}_j &= \sigma b_j(\mu_j - r_j^2) + a_j(1 + \rho_j(r_j^2 - \mu_j)),\end{aligned} \tag{62}$$

for $i = 1, \ldots, N$. Here, a_j and b_j are Cartesian coordinates of the jth oscillator with $r_j^2 = a_j^2 + b_j^2$, $K = 0.62$ is the coupling strength, and $u(t)$ is a common input to each oscillator. System parameters are taken to be $\mu_j = -3 + (j-1)/9$, $\sigma = 0.1$, and $\rho_j = 0.2 - (j-1)/9$. The output for this model is taken to be identical to the state, i.e., $y = \begin{bmatrix} a_1 & b_1 & \ldots & a_N & b_N \end{bmatrix}^T$.

For the individual elements of (62), without coupling a Hopf bifurcation occurs when $\mu_j = 0$. Here $\mu_j < 0$ for all j so that a stable fixed point results at $a_j = b_j = 0$ when $u(t) = 0$. Linearizing about this fixed point yields 10 pairs of complex-conjugate eigenvalues. The oscillatory modes associated with these eigenvalues have natural frequencies between 1.21 and 1.59 rad/s. In particular, the eigenvalues associated with the slowest decaying mode are $\lambda_{1,2} = -0.015 \pm 1.32i$ with a resonant peak near 1.32 rad/s; the eigenvalues associated with the next slowest decaying mode are $\lambda_{3,4} = -0.23 \pm 1.21$. Panel A of Fig. 2 shows the forced response of this model to the input $u(t) = 0.8\sin(1.4t)$ from panel B. In

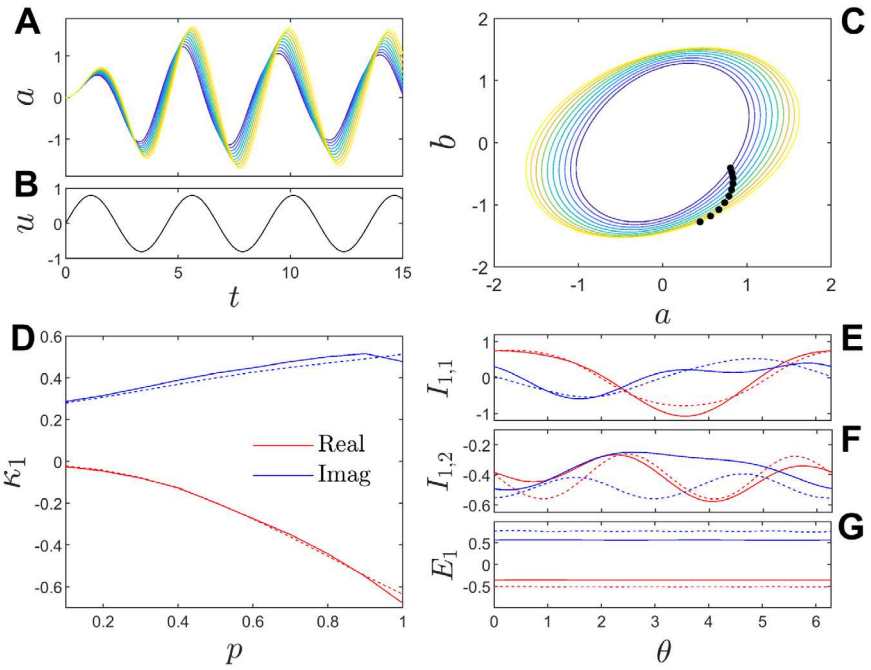

Fig. 2. For the model (62), Panel A shows individual traces of a_i in response to the sinusoidal input $u(t) = 0.8\sin(1.4t)$ from panel B. In response to continuous application of the sinusoidal forcing, the dynamics settle to a forced periodic orbit. Traces of the individual oscillators on this orbit are shown in panel C with dots indicating the location at $\theta = 0$. For a collection of orbits described in the text, the proposed data-driven model identification strategy is applied to the model. Panels D-G provide a representative sample of the information inferred from this procedure (solid lines). These terms are also compared to the ground truth which is computed directly with knowledge of the model equations (dashed lines). Panel D shows the Floquet exponent as a function of p. Panels E, F, and G, show $I_{1,1}(\theta)$, $I_{1,2}(\theta)$, and $E_1(\theta)$, respectively, obtained for the $p = 0.8$ orbit.

response to this input, the system settles to a stable, forced periodic orbit. Traces of the individual oscillators on this orbit are shown in panel C. The proposed data-driven model identification strategy from Section 3.3 is applied to the model (62) to obtain a reduced order model. The steps from Section 3.6 are followed as described below: **Step (1)** The steady state for this model is $a_j = b_j = 0$ for all j when $u(t) = 0$. The resonant frequency is 1.32 rad/s which can be seen from λ_1 but could also be approximated by applying sinusoidal input at various frequencies and measuring the maximal response. Only two Floquet coordinates are considered here so that $\beta = 2$. **Step (2)** Inputs $u(t) = p_k \sin(\omega_k t)$ for $k = 1, \ldots, 10$ are used for model identification. Here, $p_k = 0.1k$ is the magnitude of the input. The frequency $\omega_1 = 1.06$ is chosen to be slightly slower than the resonant frequency. On subsequent iterations, $\omega_{k+1} = \omega_k + 0.1(\pi/2 - \text{Imag}(\kappa_1)T)$ where κ_1 is the Floquet exponent inferred from kth limit cycle considered in the model identification process. Further discussion of this choice for the frequencies appears in Note 1 from Section 3.6. **Step 3)** inputs from Step 2 are applied over multiple cycles until all transients decay in order to infer the output y_p^y associated with the limit cycle. **Step (4)** For each p-limit cycle, the input $u(t) = p_k \sin(\omega_k t) + \alpha(t)$ is applied where $\alpha(t)$ is chosen as follows: random numbers between -0.05 and 0.05 are chosen from a uniform distribution and held constant over a 0.2 unit time interval and the resulting signal is smoothed using spline interpolation. Simulations are performed for 500 time units and the resulting data is used to estimate Fourier series coefficients up to order $\mu = 2$ for $I^1_{1,1}(\theta, p)$ and $I^1_{2,1}(\theta, p)$ along with the associated Floquet exponents using the iteration described in Section 3.3.1. Results are not sensitive the initial guess for $\kappa_{1,2}$. **Step (5)** For each p-limit cycle, the input $f_\theta(t)$ is chosen as follows: random numbers between -0.15 and 0.15 are chosen from a uniform distribution and held constant over a 2 time unit interval and the resulting signal is smoothed using spline interpolation. This is used to calculate $\hat{\theta}(t)$ from Eq. (34) and the input $u(t) = p\sin(\hat{\theta}(t))$ is applied to the full system (62) in order to estimate the Fourier coefficients of $I_{j,2}(\theta, p)$ up to order $\mu = 2$. **Step (6)** Results from Steps 4 and 5 are used to determine $E_1(\theta, p)$ for each p-limit cycle according to Eq. (40).

Panels D-G of Fig. 2 provide a representative sample of the information inferred from the proposed data-driven model identification procedure. The model is simple enough so that the associated terms can also be computed numerically with knowledge of the model equations themselves, i.e., by computing the monodromy matrix associated with the periodic orbit, computing the associated Floquet exponents, finding periodic solutions of (A.3) to identify $I^1_{1,1}(\theta, p)$ and $I^1_{2,1}(\theta, p)$, and computing $E_j(\theta, p)$ directly as defined below Eq. (8). Panel D shows the Floquet exponents as a function of p with panels E, F, and G, showing $I_{1,1}(\theta)$, $I_{1,2}(\theta)$, and $E_1(\theta)$, respectively, obtained when $p = 0.8$. While not yielding a perfect match, the true values of these functions obtained through direct computation (dashed lines) are reasonably well approximated by their corresponding terms obtained from the proposed data-driven model identification strategy (solid lines).

Once the fitting is completed, the resulting reduced order model takes the form (21). The full model has 20 states. The reduced order model considers only two Floquet coordinates, ultimately requiring only two variables to describe the θ and p dynamics. Comparisons are provided with two additional data-driven model identification strategies. The first uses a Koopman model predictive control (MPC) [9] which is closely related to the extended dynamic mode decomposition algorithm [7]. Details of the general implementation of this algorithm are given in Appendix C. Here, the time step is taken to be 0.1 units with a time-delay embedding of 24 units. The functions $L_y = [y_{i-1}, \ldots, y_{i-24}]^T \in \mathbb{R}^{480}$ and $L_u = [u_{i-1}, \ldots, u_{i-24}]^T \in \mathbb{R}^{24}$ are used to lift to a higher dimensional state, defining h_i from Eq. (C.2). The same data used to obtain the model of the form (21) is used to build the matrices H and H^+ defined below Eq. (C.2) and the A and B matrices are fit according to Eq. (C.3). The length of the delay embedding for the Koopman MPC strategy is chosen with a trial-and-error process; the Koopman MPC algorithm is applied for various embedding lengths and increased until there are no discernible improvements in the accuracy of the resulting model. The second model identification strategy used for comparison was presented in [18]. Here, sinusoidal inputs of varying frequencies are applied and the resulting steady state outputs are

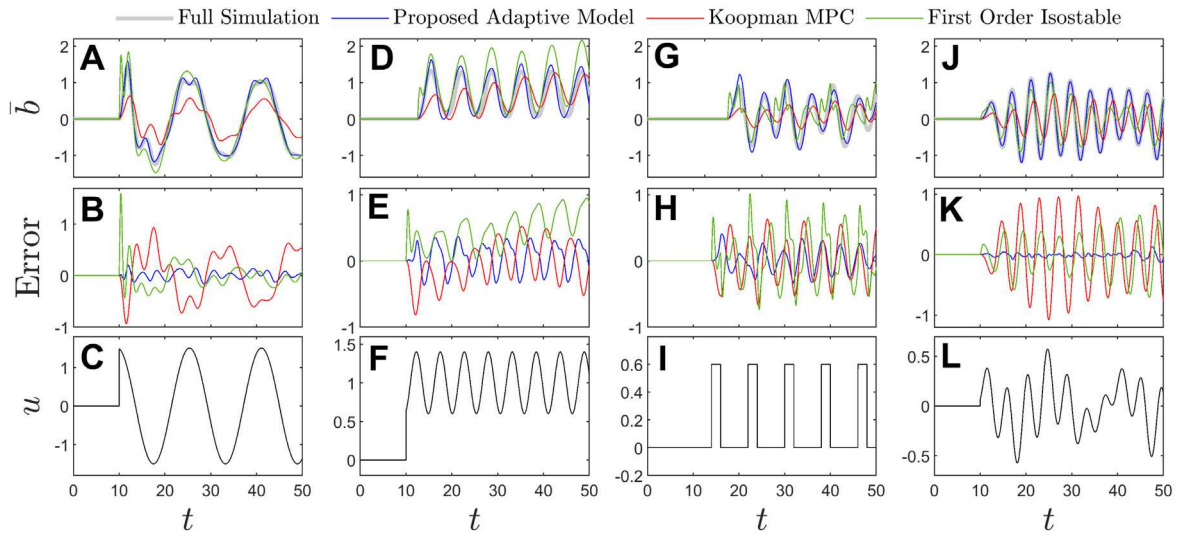

Fig. 3. The different inputs from panels C, F, I, and L are applied to the full order model (62) along with the proposed adaptive data-driven model identification strategy and two other data-driven models. Corresponding traces of $\bar{b} = \frac{1}{N}\sum_{j=1}^{N} b_j$ are shown in panels A, D, G, and J with associated errors shown in panels B, E, H, and K. The proposed model identification strategy outperforms the other strategies for all inputs shown here.

used to infer a model of the form

$$\begin{aligned} \dot{\phi}_i &= \lambda_i \phi_i + c_i u(t), \\ & i = 1 \dots r, \\ y(t) &= y_0 + \sum_{k=1}^{r} \phi_k, \end{aligned} \tag{63}$$

where $\phi \in \mathbb{C}$ is an isostable coordinate, $\lambda_i \in \mathbb{C}$ is an associated unperturbed decay rate, $c_i \in \mathbb{C}$ captures the response to input, and $y_0 \in \mathbb{R}$ is the steady state when $u(t) = 0$. Isostable coordinates can be formally defined as level sets of the slowest decaying eigenmodes of the Koopman operator [5]. The model (63) represents a reduced order model taken to first order accuracy in the expansion of a subset of the slowest decaying isostable coordinates. A more detailed description of this model identification strategy is given in [18] which explains how the model (63) can be inferred with knowledge of the steady state response to various sinusoidal inputs. Inputs of the form $u(t) = \sin(\omega t)$ with $\omega = \{0.1, 0.2, \dots, 2.0\}$ are used for the fitting with $r = 10$ isostable coordinates. The decay rates $\lambda_k = -0.2k$ are used to implement the fitting procedure. Other choices were also used that gave similar results to those presented here.

Simulations for the various reduced order models are compared to those obtained from full model simulations of (62) for different inputs with results shown in Fig. 3. A purely sinusoidal input $u(t) = 1.5\sin(0.5t)$ is shown in panel C, a positively shifted sinusoid $u(t) = 1 + 0.4\sin(1.2t)$ is shown in panel F, pulses applied every 8 time units of magnitude 0.6 are shown in panel I, and the sum of three sinusoids $u(t) = 0.15\sin(1.3t) + 0.2\sin(0.4t) + 0.5\sin(1.5t)$ is shown in panel L. The resulting value of $\bar{b} = \frac{1}{N}\sum_{j=1}^{N} b_j$ from each input is given in panels A, D, G, and J with the respective error between the full and reduced order models shown in panels B, E, H, and K. The mean absolute error, $\frac{1}{100}\int_{10}^{110} |\text{Error}(t)| dt$ over 100 time units after the inputs are applied is given below: for the purely sinusoidal input from panel C, the shifted sine wave in panel F, pulse input from panel I, and mixed sinusoidal input from panel L the average error is (0.06, 0.41, 0.14), (0.20, 0.25, 0.61), (0.11, 0.25, 0.35), and (0.03, 0.50, 0.30) for the proposed adaptive method, Koopman MPC, and first order isostable method respectively. The proposed model identification strategy gives a better match than the other two model identification strategies. Note that none of the testing inputs were seen during training; the purely sinusoidal input has a substantially slower natural frequency and higher magnitude than the inputs used for training.

4.2. Spike rate of a coupled neural population

Neural rhythms result from the complex interplay between individual neural dynamics, synaptic coupling between neurons, and inputs from upstream neural populations. Due to the inherent complexity of these systems, rather than examining individual neurons, it can be more useful to examine the aggregate behavior, for instance, capturing the dynamics of the firing rate, mean membrane potential, or other population characteristics [38–41]. Phase-based reduction techniques have been considered population-level analysis of neural populations [35,42–45], but it is generally unclear how to apply phase-based approaches when the underlying model does not produce aggregate oscillations in the absence of other external input. With these considerations in mind, the proposed data-driven model identification strategy is illustrated for a population of $N = 1000$ synaptically coupled, tonically firing, conductance-based neurons taken from [46]. Model equations are of the form

$$\begin{aligned} C\dot{V}_i &= -I_{\text{L}}(V_i) - I_{\text{Na}}(V_i, h_i) - I_{\text{K}}(V_i, h_i) - I_{\text{T}}(V_i, r_i) \\ &\quad + I_i^b - \frac{g_{\text{syn}}}{N}\sum_{j=1}^{N} s_j(V_i - E_{\text{syn}}) + \sqrt{2D}\eta_i(t) + u(t), \\ \dot{h}_i &= (h_\infty(V_i) - h_i)/\tau_h(V_i), \\ \dot{r}_i &= (r_\infty(V_i) - r_i)/\tau_r(V_i), \\ \dot{s}_i &= \frac{a(1-s)}{1 + \exp(-(V_i - V_T)/\sigma_T)} - bs_i, \end{aligned} \tag{64}$$

for $i = 1, \dots, N$. Above, V_i is the transmembrane voltage of neuron i, h_i, and r_i are associated gating variables, and s_i is a synaptic variable used to set the synaptic current. The synaptic conductance is $g_{\text{syn}} = 0.4$ mS/cm^2 and the neurons are coupled in an all-to-all manner. $E_{\text{syn}} = 0$ mV so that the synaptic connections are excitatory with additional parameters $a = 3$, $V_T = -20$ mV, $\sigma_T = 0.8$ mV, and $b = 1$ determining the dynamics of the synaptic variable. $u(t)$ is an applied current that is identical for each neuron, and $C = 1$ μF/cm^2 is the membrane capacitance. The term $\sqrt{2D}\eta_i(t)$ represents an independent and identically distributed zero-mean white noise process with intensity $D = 1$. The baseline current I_i^b is drawn from a normal distribution with mean 5 and variance 1 μA/cm^2. Additional ionic currents $I_{\text{L}}, I_{\text{Na}}, I_{\text{K}}$, and I_{T}, and auxiliary functions $h_\infty, r_\infty, \tau_h$, and τ_r are identical to those from [46].

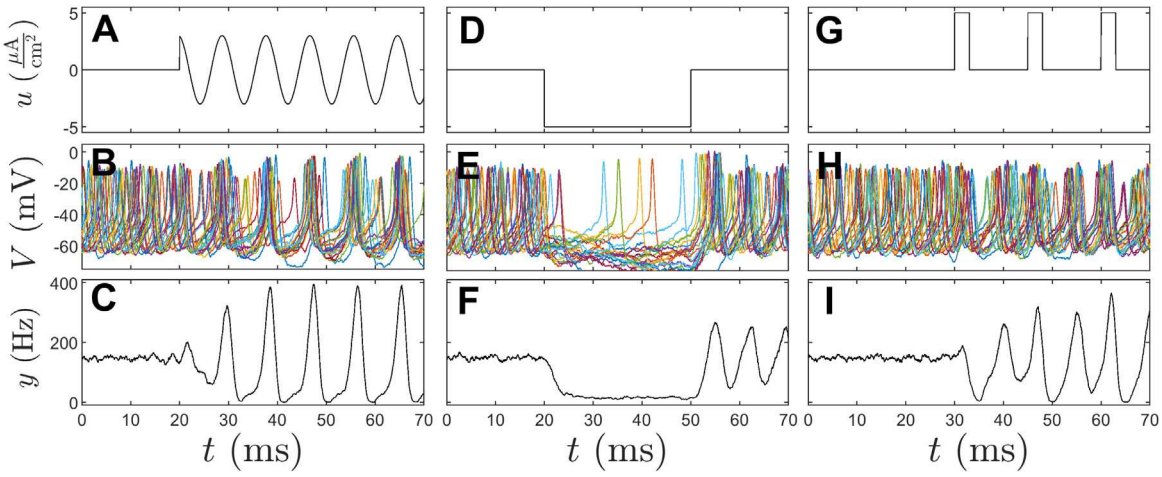

Fig. 4. The collective behavior of the neuron population from (64) is shown in response to inputs. The inputs are shown in panels A, D, and G. Panels B, E, and H, respectively, show a representative sampling of transmembrane voltages of individual neurons from the population in response to these inputs. Panels C, F, and I, respectively, show the firing rate computed according to Eq. (65). When $u(t) = 0$, $y(t)$ tends towards a firing rate of about 144 Hz. The goal in this example is to identify a model that captures the firing rate $y(t)$ in response to general inputs $u(t)$ using the method described in Section 3.1.

The firing rate for the model (64) is taken as the single model observable, defined as

$$y = \frac{1}{W}\sum_{j=1}^{N} A_i(t, W), \tag{65}$$

where $A_i = 1$ if neuron i has fired an action potential in the window $[t, t - W]$ and 0 otherwise. Here, neuron i is defined to fire an action potential when V_i crosses a threshold of -25 mV with a positive slope and $W = 1.5$ ms. Fig. 4 shows the general behavior of the model (64) in response to various inputs. When $u(t) = 0$, the model tends towards a constant firing rate $y(t) \approx 144$ Hz. The inputs shown in panels A, D, and G yield the outputs shown in panels C, F, and I, respectively. In panels B, E, and H, a representative subset of the transmembrane voltages of neurons in the population is shown giving a sense of the aggregate behavior in response to the inputs. Notice the strong resonance with the periodic input in panel A, which is characteristic of systems with a complex-conjugate eigenvalue.

The proposed data-driven model identification methodology from Section 3.3 is applied to the model (64) in order to provide a low order representation that can accurately predict the dynamics that map the input to the output. The steps from Section 3.6 are followed as described below: **Step (1)** The steady state for this model is taken to be $y = 144$ Hz which results in the limit that $u(t) = 0$. Note that due to noise, the model does not asymptote its steady state value. The resonant frequency is estimated to be approximately 0.8 rad/s by applying a sinusoidal input at various frequencies and measuring the maximal response. Only two total Floquet coordinates are considered, i.e., taking $\beta = 2$. **Step (2)** An input $u(t) = p\sin(0.7t)$ is applied where $p = \{0.5, 1.0, \ldots, 6.0\}$ to define a collection of 12 periodic orbits used for the reduction. Other frequencies could also be chosen provided they are near the resonant frequency. Further discussion of the choice in the frequency of the applied input is provided in Note 1 from Section 3.6. **Step (3)** The input from Step 2 is applied over multiple cycles and the output is averaged to obtain an approximation of each output y_p^γ associated with the limit cycle. **Step (4)** For each p-limit cycle, an input $u(t) = p\sin(0.7t) + \alpha(t)$ is applied where $\alpha(t)$ is chosen as follows: random numbers between -0.6 and 0.6 are chosen from a uniform distribution and held constant over a 2 ms time interval and the resulting signal is smoothed using spline interpolation. Simulations are performed for $t \in [0, 3000]$ ms. The resulting data is used to estimate the Fourier series coefficients up to order $\mu = 2$ for $I^1_{1,1}(\theta, p)$ and $I^1_{2,1}(\theta, p)$ along with the associated Floquet exponents using the iteration described in Section 3.3.1. Initial guesses for the Floquet exponents taken to be $\kappa_{1,2} = -0.06 \pm 0.8i$. The results are not sensitive to this initial guess provided $\mathrm{Imag}(\kappa_1)$ for the guess is close to the resonant frequency for this system. **Step (5)** For each p-limit cycle, pulses are chosen for $f_\theta(t)$ of the form

$$f_\theta(t) = \begin{cases} 5, & \text{if } \mathrm{mod}(t, 16.5) < 0.075, \\ 0, & \text{otherwise.} \end{cases} \tag{66}$$

Considering the associated $\hat{\theta}(t)$ phase dynamics from Eq. (34), this corresponds to rapid shifts in $\hat{\theta}(t)$ by 0.375 radians occurring every 16.5 ms. The input $u(t) = p\sin(\hat{\theta}(t))$ is applied to the full system (64) and the resulting outputs are used to estimate the Fourier coefficients of $I_{j,2}(\theta, p)$ up to order $\mu = 2$. **Step (6)** Results from Steps 4 and 5 are used to determine $E_1(\theta, p)$ for each p-limit cycle according to Eq. (40). Fig. 5 shows the functions that are obtained from this process. Panel A shows the resulting periodic orbits for different values of p. The associated Floquet exponents are shown in panel B. The real component of the Floquet exponent decreases as the magnitude of the input increases indicating that the orbit becomes more strongly attracting. Panels C and D show the real and imaginary components of $E_1(\theta, p)$ inferred from the fitting procedure.

Once the fitting is completed, the resulting reduced order model takes the form (21). In this case, only two Floquet coordinates are considered so that the reduced order model only requires two variables to describe the θ and p dynamics. This is a significant reduction from the 4000 variables contained in the full order model (64). Comparisons are provided with two additional data-driven model identification strategies. The first uses Koopman model predictive control (MPC) [9]. Details of the general implementation of this algorithm are given in Appendix C; here the time step is taken to be 0.15 ms with a time-delay embedding of 49 units. The functions $L_y = [y_{i-1}, \ldots, y_{i-49}]^T \in \mathbb{R}^{49}$ and $L_u = [u_{i-1}, \ldots, u_{i-49}]^T \in \mathbb{R}^{49}$ are used to lift to a higher dimensional state by defining h_i from Eq. (C.2). The same data used to obtain the model of the form (21) is used to build the matrices H and H^+ defined below Eq. (C.2) and the associated A and B matrices are fit according to Eq. (C.3). The length of the delay embedding for the Koopman MPC strategy is chosen with a trial-and-error process; the Koopman MPC algorithm is applied for various embedding lengths and increased until there are no discernible improvements in the accuracy of the resulting model. The second model identification strategy used for comparison was presented in [18]. Here, sinusoidal inputs of varying frequencies are applied and the resulting steady state outputs are used to infer a model of the form (63) which was explained in further detail in Section 4.1. For this comparison model identification strategy, inputs

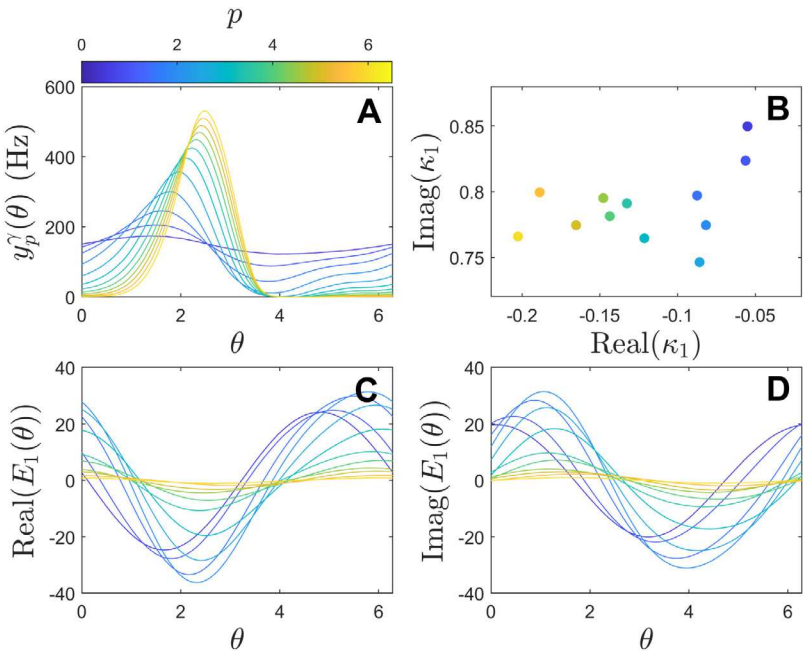

Fig. 5. A sampling of the curves obtained from the proposed model-identification procedure. Panel A shows $y_p^\gamma(\theta)$, i.e., the observable on the p-limit cycle for different values of p. The inferred Floquet multipliers are shown in Panel B. Panels C and D show $E_1(\theta, p)$ as obtained from the fitting procedure for different values of p. This term captures how the Floquet coordinates change in response to shifts in the parameter p.

of the form $u(t) = \sin(\omega t)$ with $\omega = \{0.3, 0.4, \ldots, 1.2\}$ are used for the fitting with $r = 10$ isostable coordinates having decay rates $\lambda_k = -0.2k$. Other choices were also used that gave similar results to those shown here.

Simulations for the various reduced order models are compared to those obtained from full model simulations of (64) for different inputs with results shown in Fig. 6. A sinusoidal input $u(t) = \sin(0.83t)$ which is close to the resonant frequency shown in Panel C, a $u = -5$ μA/cm^2 pulse applied for 30 ms is shown in panel F, pulses of amplitude $u = 5$ μA/cm^2 applied every 15 ms are shown in panel I, and the input $u(t) = 1.53\sin(0.6t) + 1.19\cos(0.7t) + 2.21\cos(0.3t)$ μA/cm^2 is shown in panel L. Corresponding outputs from each input are shown in panels A, D, G, and J with the respective error between full and reduced order simulations given in panels B, E, H, and K. The mean absolute error, $\frac{1}{100}\int_{20}^{120} |\text{Error}(t)|dt$, is also provided for each model giving a quantitative measure of the error for each model for the first 100 ms after input is first applied. For the purely sinusoidal input in panel C, single pulse in panel F, multiple pulse input from panel I, and mixed sinusoidal input from panel L the average error is (19.2, 45.0, 31.9) Hz, (24.0, 63.3, 54.3) Hz, (30.3, 82.4, 71.9) Hz, and (21.7, 50.0, 67.0) Hz for the proposed adaptive method, Koopman MPC, and first order isostable model, respectively. For each input, the proposed adaptive method gives between 40 and 60 percent less error than the next best model. Additionally, the proposed model identification strategy always provides results that are qualitatively similar to the full order model while the other reduced order models often provide results that are substantially different.

5. Conclusion

In this work, a data-driven model identification strategy is presented that considers the dynamics of a general nonlinear system in reference to a collection of externally forced periodic orbits. By inferring information about the phase–amplitude dynamics of the individual periodic orbits, a low-order model can be obtained that accurately captures the dynamics of the underlying model in response to arbitrary external inputs. This work provides an extension for the strategy presented in [25] which required explicit knowledge of the underlying model equations. By contrast, the model identification procedure summarized in Section 3.6 only requires the ability to apply inputs and measure the resulting time-series data. In examples considered in Section 4, the proposed technique outperforms both Koopman model predictive control [9] and an isostable-coordinate-based model identification strategy from [18].

As compared to DMD [1–3] and its variants [7–9], the proposed model identification strategy places some structure on the underlying equations, learning a representation of the system based on the dynamics of the underlying periodic orbits. Specifying the underlying structure likely mitigates the risk of overfitting to data and provides a better representation of the overall system dynamics. As compared to other data-driven model identification strategies that attempt to learn the model equations that generate snapshot data, [10–13], the proposed model identification strategy provides a universal representation based on the phase and amplitude dynamics of the underlying forced periodic orbits. The resulting model does not require a specification of a function library and can be implemented without the need for machine learning. Nonetheless, it may be of interest to consider more sophisticated fitting strategies in the model identification procedure in order to yield better approximations of the phase–amplitude reduced order dynamics.

While the preliminary results presented here are promising, this strategy still has a number of limitations. Foremost, it is explicitly assumed that the dynamics of the underlying system (10) approach a stable periodic orbit in response to the applied input $u(t)$. This is guaranteed in the limit of weak forcing for systems with a stable fixed point, even when the associated eigenvalues of the linearized fixed point are purely real. However, as the magnitude of the periodic forcing increases, periodic orbits may not persist as the magnitude of the forcing becomes larger. This limitation would likely preclude implementation for systems displaying chaotic dynamics where stable periodic orbits would not be observed, but potentially could be overcome by incorporating chaos control strategies [47–49] to stabilize the resulting unstable orbits so that the necessary data can be collected for model fitting. Additionally, in the implementation of the proposed strategy, the extended phase and extended isostable coordinates from Eq. (16) associated with the periodic orbit X_p^γ must be continuous with respect

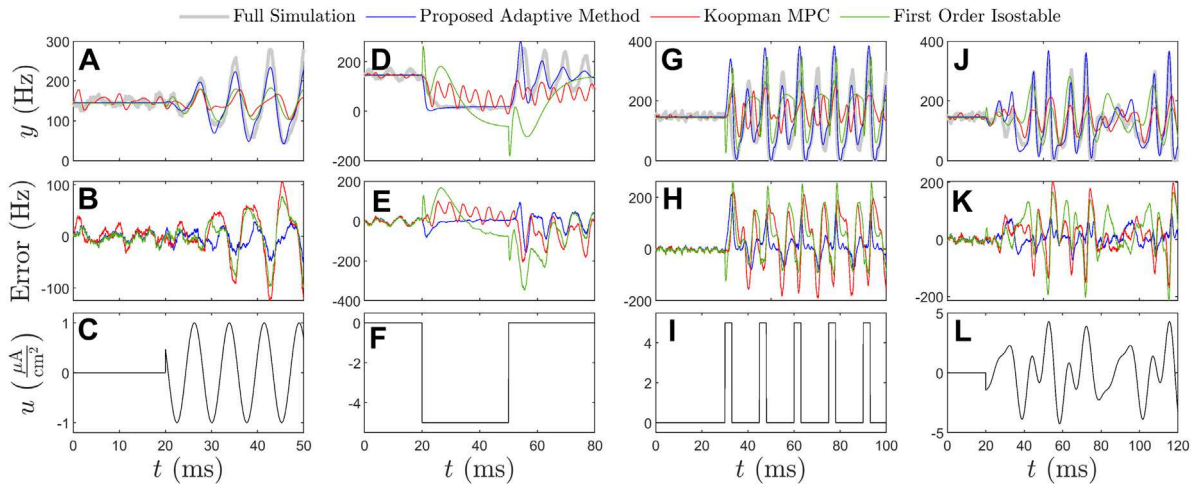

Fig. 6. The inputs from panels C, F, I, and L are applied to the full order model (64), the proposed adaptive data-driven model identification strategy, and two other data-driven models. Corresponding output traces are shown in panels A, D, G and J with associated errors shown in panels B, E, H, and K. In addition to giving the correct qualitative behavior, the proposed adaptive reduction strategy yields a model with approximately half as much error as the other two comparison data-driven strategies. Note that the proposed method was not trained on any of the test inputs from Fig. 6; the pure sine wave in panel C has different frequency than the sinusoidal inputs used for training.

to p (the amplitude of the periodic forcing). This precludes critical points of p for which a bifurcation occurs from the allowable parameter set. In order to consider forced vibration problems, for instance, with a system having regions of phase space with qualitatively different dynamics separated by homoclinic orbits [50], further extensions to the proposed model identification strategy would be necessary.

The proposed model identification strategy exploits rapid convergence of some of the Floquet coordinates in order to arrive at a low-order representation for the model dynamics. In principle, it can accommodate the influence of an arbitrary number of low amplitude, slowly decaying modes, but in practice it may be difficult to distinguish the influence from each of these modes using data, especially for Floquet exponents that are close to each other. Additionally, adding more low amplitude modes will not necessarily guarantee a more accurate model. With this in mind, it would be worthwhile to extend this data-driven procedure to accommodate additional pairs of large amplitude oscillatory modes. In this work, the influence of noise and measurement error is not explicitly considered here which may decrease the accuracy of the proposed model identification strategy. Some of these concerns are at least partially alleviated by the results for the neural system from Eq. (64); even for a large scale and noisy model, the two-mode reduced order model performs well in this example, especially compared to the other data-driven model identification strategies considered.

CRediT authorship contribution statement

Dan Wilson: Conceptualization, Formal analysis, Funding acquisition, Investigation, Methodology, Validation, Visualization, Writing – original draft, Writing – review & editing.

Declaration of competing interest

The author declares that there is no conflict of interest to report.

Data availability

Data will be made available on request.

Acknowledgment

This material is based upon the work supported by the National Science Foundation (NSF) under Grant No. CMMI-2140527.

Appendix A. Numerical computation of terms comprising the adaptive phase-amplitude reduced order equations

Consider a general equation of the form (12) with a forced periodic orbit of the form (13) that results for a constant choice of p when taking $u(t) = 0$. If the underlying equations are known, the terms comprising the adaptive phase–amplitude reduced order equations can be computed numerically. For instance, the gradient of the phase $a(\theta, p) \equiv \frac{\partial \theta}{\partial X}$ evaluated on the periodic orbit X_p^γ can be obtained by computing periodic solutions of the adjoint equation [28,51],

$$\dot{a} = -\boldsymbol{J}^T a, \tag{A.1}$$

where $\boldsymbol{J}$ is the Jacobian evaluated at X_p^γ normalized so that

$$\frac{2\pi}{T(p)} = \begin{bmatrix} F_x(x_p^\gamma(\theta), pf(\theta)) \\ \omega \end{bmatrix} \cdot a(\theta, p), \tag{A.2}$$

where the dot denotes the dot product. Likewise, as discussed in [33,34], $b_j(\theta, p) \equiv \frac{\partial \psi_j}{\partial X}$ evaluated on the periodic orbit x_p^γ can be computed by finding periodic solutions of

$$\dot{b}_j = -(\boldsymbol{J}^T - \kappa_j \mathrm{Id}) b_j, \tag{A.3}$$

where κ_j is the Floquet exponent associated with the Floquet coordinate ψ_j and Id is an appropriately sized identity matrix. Corresponding Floquet eigenfunctions $g_j(\theta, p)$ can be computed by finding periodic solutions of

$$\dot{g}_j = (\boldsymbol{J} - \kappa_j \mathrm{Id}) g_j. \tag{A.4}$$

Additionally, the resulting $g_j(\theta, p)$ and $b_j(\theta, p)$ must be scaled so that $g_k^T(\theta, p) b_j(\theta, p) = 1$ if $k = j$ and 0 otherwise. As discussed in [34], the relationship

$$b_j^T(\theta, p) \frac{dX_p^\gamma}{dt} = 0, \tag{A.5}$$

must also be satisfied for all states on the periodic orbit for all j.

Appendix B. Reduced order terms comprising the adaptive reduction in the limit of weak forcing

Ref. [25] derived explicit representations for the terms of an adaptive reduction of the form (16) for oscillations that result from a carefully designed input added directly to the state equation. By contrast, in the current work, general periodic inputs are considered to yield forced periodic orbits used in the adaptive reduction. Nonetheless,

in the limit of weak forcing, the terms of the adaptive reduction have a shared structure. This point is illustrated below following a similar derivation to the one given in Section 3.2 of [25].

To begin, consider the T-periodic linear time varying Eq. (49) that characterizes solutions near the periodic orbit of (12) that results from the periodic input $pf(t)$ when taking $u(t) = 0$. Note that while (49) is linear time varying, this equation becomes linear time invariant when truncating the $O(\epsilon)$ terms. As such, the monodromy matrix Φ that solves $\Delta X(T) = \Phi X(0)$ can be approximated to leading order as

$$\begin{aligned}\Phi &= e^{\left(\begin{bmatrix} A & 0 \\ 0 & 0 \end{bmatrix}T\right)} + O(\epsilon) \\ &= \begin{bmatrix} e^{AT} & 0 \\ 0 & 1 \end{bmatrix} + O(\epsilon) \\ &= \Phi_0 + O(\epsilon),\end{aligned} \tag{B.1}$$

where Φ_0 contains the $O(1)$ terms of the monodromy matrix. Above, the structure in the second line follows directly from the diagonal structure of the $O(1)$ terms.

Eigenvalues λ_j^{Φ} and associated left and right eigenvalues w_j^{Φ} and v_j^{Φ}, respectively, of Φ can be used to determine the Floquet multipliers and Floquet eigenfunctions of the periodic orbit defined in (13). As discussed in Appendix B of [25], the eigenvalues and eigenvectors of Φ_0 ($\lambda_j^{\Phi_0}$, $w_j^{\Phi_0}$, and $v_j^{\Phi_0}$) will be $O(\epsilon)$ approximations of λ_j^{Φ}, w_j^{Φ}, and v_j^{Φ} provided $\lambda_j^{\Phi_0}$ is simple. With this in mind and considering Eq. (B.1), for any eigenvalue, right eigenvector, and left eigenvector triple (λ_j, v_j, w_j) of A

$$v_j^{\Phi_0} = \begin{bmatrix} v_j \\ 0 \end{bmatrix} \tag{B.2}$$

is a right eigenvector of Φ_0 with eigenvalue $\lambda_j^{\Phi_0} = \exp(\lambda_j T)$. It is also straightforward to verify that

$$w_j^{\Phi_0} = \begin{bmatrix} w_j \\ 0 \end{bmatrix} \tag{B.3}$$

is a right eigenvector of Φ_0^T with corresponding eigenvalue $\lambda_j^{\Phi_0}$ and hence is a left eigenvector of Φ_0. The Floquet exponent for the periodic orbit (13) corresponding to $\lambda_j^{\Phi_0}$ is

$$\begin{aligned}\kappa_j &= \frac{\log(\exp(\lambda_j T))}{T} + O(\epsilon) \\ &= \frac{\log|\exp(\lambda_j T)|}{T} + i\frac{\arg(\exp(\lambda_j T))}{T} + O(\epsilon) \\ &= \mathrm{Real}(\lambda_j) + i\mathrm{Imag}(\lambda_j) - \frac{2\pi i m}{T} + O(\epsilon).\end{aligned} \tag{B.4}$$

Above, because $\exp(a+bi) = \exp(a+bi+2k\pi i)$ for any integer value of k, the additional term $2\pi i m/T$ is chosen appropriately with the mandate that $\mathrm{Imag}(\log(\exp(\lambda_j T))) \in (-\pi, \pi]$. The Floquet eigenfunction $g_j(\theta, p)$ associated with the Floquet multiplier κ_j can be obtained by finding periodic solutions to Eq. (A.4); to leading order ϵ, substituting Eq. (48) for the Jacobian this equation becomes

$$\dot{g}_j = \left(\begin{bmatrix} A & 0 \\ 0 & 0 \end{bmatrix} - \kappa_j \mathrm{Id}\right) g_j + O(\epsilon). \tag{B.5}$$

For any $g_j \propto \begin{bmatrix} v_j^T & 0 \end{bmatrix}^T$, Eq. (B.5) simplifies to

$$\begin{aligned}\dot{g}_j &= g_j(\lambda_j - \kappa_j) + O(\epsilon) \\ &= g_j 2\pi i m/T + O(\epsilon).\end{aligned} \tag{B.6}$$

Above, the first line is obtained by recalling that v_j is an eigenvalue of A and the second line is obtained by substituting (B.4). Integrating Eq. (B.5) over one period ultimately yields the solution

$$g_j = \begin{bmatrix} v_j \\ 0 \end{bmatrix} \exp(\omega i m t) + O(\epsilon), \tag{B.7}$$

with the substitution $\omega = 2\pi/T$. Likewise, the gradient of the Floquet coordinates with respect to the state can be computed by finding periodic solutions of (A.3). Substituting the relevant terms, to leading order this equation is

$$\dot{b}_j = -\left(\begin{bmatrix} A^T & 0 \\ 0 & 0 \end{bmatrix} - \kappa_j \mathrm{Id}\right) b_j + O(\epsilon). \tag{B.8}$$

For any $b_j \propto \begin{bmatrix} w_j^T & 0 \end{bmatrix}^T$, Eq. (B.8) simplifies to

$$\begin{aligned}\dot{b}_j &= -b_j(\lambda_j - \kappa_j) + O(\epsilon) \\ &= -b_j 2\pi i m/T + O(\epsilon).\end{aligned} \tag{B.9}$$

Noting that $w_j^{\Phi_0}$ from (B.3) provides an initial condition that solves (B.8) to leading order ϵ, integrating (B.9) over one period ultimately yields solutions of the form (recall that $\frac{\partial \psi_j}{\partial X} \equiv b_j$)

$$b_j(t) = \begin{bmatrix} w_j \exp(-\omega i m t) + O(\epsilon) \\ b_{j,2}(t) \end{bmatrix}, \tag{B.10}$$

where $b_{j,2}(t)$ is a T-periodic $O(\epsilon)$ term. The term $b_{j,2}(t)$ can be determined by considering (A.5), specifically

$$\begin{aligned}0 &= b_j^T(\theta, p)\frac{dX_p^{\gamma}}{dt} \\ &= \begin{bmatrix} w_j^T \exp(-\omega i m t) + O(\epsilon) & b_{j,2}(t) \end{bmatrix} \\ &\quad \times \begin{bmatrix} p\frac{d}{dt}\left(e^{At}x_0 + \int_0^t e^{A(t-\tau)}Bf(\omega\tau)d\tau\right) \\ \omega \end{bmatrix},\end{aligned} \tag{B.11}$$

where terms $O(\epsilon^2)$ and higher are truncated and the second line is obtained by substituting (B.10) for b_j and (45) for x_p^{γ} to leading order ϵ. Solving (B.11) for $b_{j,2}(t)$ ultimately yields

$$b_{j,2}(t) = p\eta_j(t), \tag{B.12}$$

where

$$\eta_j(t) = -\frac{1}{\omega} w_j^T \exp(-\omega i m t)\frac{d}{dt}\left(e^{At}x_0 + \int_0^t e^{A(t-\tau)}Bf(\omega\tau)d\tau\right). \tag{B.13}$$

Note that $b_{j,2} \equiv \frac{\partial \psi_j}{\partial s}$. Of particular importance, note that $b_{j,2}(t)$ is directly proportional to p.

Appendix C. Koopman model predictive control algorithm

The proposed model identification algorithm is compared to the Koopman model predictive control algorithm from [9] (cf., [52]). Considering the general model of the form (10), Koopman model predictive control considers a series of data snapshots

$$s_i = (y_i, y_i^+, u_i), \tag{C.1}$$

where $y_i = y(x(t_i)) \in \mathbb{R}^K$, $y_i^+ = y(x(t_i + \Delta t)) \in \mathbb{R}^K$, and $u_i = u(t_i) \in \mathbb{R}^M$, with Δt being a constant timestep. A lifted state vector is generally considered

$$h_i = \begin{bmatrix} y_i \\ L_y(y_i, y_{i-1}, y_{i-2}, \dots) \\ L_u(u_{i-1}, u_{i-2}, \dots) \end{bmatrix}, \tag{C.2}$$

where L_y and L_u are vectors comprised of the current and previous outputs and previous inputs, respectively. The augmentation of the current state with additional information about the time history is often referred to as time-delay embedding [8]. Note that the time-delay embedding is not explicitly required to implement the Koopman model predictive control algorithm. The goal of the Koopman model predictive control approach is to obtain an approximation for the linear relationship $h_i^+ = Ah_i + Bu_i$. Letting $H = \begin{bmatrix} h_1 \dots h_d \end{bmatrix}$, $H^+ = \begin{bmatrix} h_1^+ \cdots h_d^+ \end{bmatrix}$, and $U = \begin{bmatrix} u_1 \dots u_d \end{bmatrix}$ where d is the total number of pairs of lifted state

coordinates, a least squares fit for A and B can be obtained according to

$$\begin{bmatrix} A & B \end{bmatrix} = H^{+} \begin{bmatrix} H \\ U \end{bmatrix}^{\dagger}, \tag{C.3}$$

where † denotes the pseudoinverse. At each step, predictions for the observable can be obtained from the first K entries of h_i. The Koopman model predictive control algorithm is closely related to extended dynamic mode decomposition [7] and other techniques involving dynamic mode decomposition [53]. This approach is distinct from standard linearization around a reference point or trajectory; because of its close connection to the Koopman operator, it can be thought of as a global linearization of the underlying dynamical system.

References

[1] P.J. Schmid, Dynamic mode decomposition of numerical and experimental data, J. Fluid Mech. 656 (2010) 5–28.
[2] J.N. Kutz, S.L. Brunton, B.W. Brunton, J.L. Proctor, Dynamic Mode Decomposition: Data-Driven Modeling of Complex Systems, Society for Industrial and Applied Mathematics, Philadelphia, PA, 2016.
[3] J.H. Tu, C.W. Rowley, D.M. Luchtenburg, S.L. Brunton, J.N. Kutz, On dynamic mode decomposition: Theory and applications, J. Comput. Dyn. 1 (2) (2014) 391–421.
[4] M. Budišić, R. Mohr, I. Mezić, Applied Koopmanism, Chaos 22 (4) (2012) 047510.
[5] I. Mezić, Analysis of fluid flows via spectral properties of the Koopman operator, Annu. Rev. Fluid Mech. 45 (2013) 357–378.
[6] I. Mezić, Spectrum of the Koopman operator, spectral expansions in functional spaces, and state-space geometry, J. Nonlinear Sci. (2019) 1–55.
[7] M.O. Williams, I.G. Kevrekidis, C.W. Rowley, A data–driven approximation of the Koopman operator: Extending dynamic mode decomposition, J. Nonlinear Sci. 25 (6) (2015) 1307–1346.
[8] H. Arbabi, I. Mezic, Ergodic theory, dynamic mode decomposition, and computation of spectral properties of the Koopman operator, SIAM J. Appl. Dyn. Syst. 16 (4) (2017) 2096–2126.
[9] M. Korda, I. Mezić, Linear predictors for nonlinear dynamical systems: Koopman operator meets model predictive control, Automatica 93 (2018) 149–160.
[10] S.L. Brunton, J.L. Proctor, J.N. Kutz, Discovering governing equations from data by sparse identification of nonlinear dynamical systems, Proc. Natl. Acad. Sci. 113 (15) (2016) 3932–3937.
[11] S.H. Rudy, S.L. Brunton, J.L. Proctor, J.N. Kutz, Data-driven discovery of partial differential equations, Sci. Adv. 3 (4) (2017) e1602614.
[12] N.M. Mangan, T. Askham, S.L. Brunton, J.N. Kutz, J.L. Proctor, Model selection for hybrid dynamical systems via sparse regression, Proc. R. Soc. Lond. Ser. A Math. Phys. Eng. Sci. 475 (2223) (2019) 20180534.
[13] H. Schaeffer, Learning partial differential equations via data discovery and sparse optimization, Proc. R. Soc. A 473 (2197) (2017) 20160446.
[14] M. Raissi, P. Perdikaris, G.E. Karniadakis, Machine learning of linear differential equations using Gaussian processes, J. Comput. Phys. 348 (2017) 683–693.
[15] M. Raissi, P. Perdikaris, G.E. Karniadakis, Numerical66 Gaussian processes for time-dependent and nonlinear partial differential equations, SIAM J. Sci. Comput. 40 (1) (2018) A172–A198.
[16] S. Cuomo, V.S. Di Cola, F. Giampaolo, G. Rozza, M. Raissi, F. Piccialli, Scientific machine learning through physics–informed neural networks: where we are and what's next, J. Sci. Comput. 92 (3) (2022) 88.
[17] T. Ahmed, A. Sadovnik, D. Wilson, Data-driven inference of low-order isostable-coordinate-based dynamical models using neural networks, Nonlinear Dynam. 111 (3) (2023) 2501–2519.
[18] D. Wilson, Data-driven inference of high-accuracy isostable-based dynamical models in response to external inputs, Chaos 31 (6) (2021) 063137.
[19] D. Wilson, A direct method approach for data-driven inference of high accuracy adaptive phase-isostable reduced order models, Physica D (2023) 133675.
[20] D. Wilson, A data-driven phase and isostable reduced modeling framework for oscillatory dynamical systems, Chaos 30 (1) (2020) 013121.
[21] A. Mauroy, I. Mezić, J. Moehlis, Isostables, isochrons, and Koopman spectrum for the action–angle representation of stable fixed point dynamics, Physica D 261 (2013) 19–30.
[22] E. Kaiser, J.N. Kutz, S. Brunton, Data-driven discovery of Koopman eigenfunctions for control, Mach. Learn.: Sci. Technol. (2021).
[23] D. Wilson, An adaptive phase-amplitude reduction framework without $\mathcal{O}(\epsilon)$ constraints on inputs, SIAM J. Appl. Dyn. Syst. 21 (1) (2022) 204–230.
[24] D. Wilson, S.M. Djouadi, Adaptive isostable reduction of nonlinear PDEs with time varying parameters, IEEE Control Syst. Lett. 5 (1) (2021) 187–192.
[25] D. Wilson, K. Sun, Reduced order characterization of nonlinear oscillations using an adaptive phase-amplitude coordinate framework, 2023, arXiv preprint 2302.03016.
[26] J. Guckenheimer, Isochrons and phaseless sets, J. Math. Biol. 1 (3) (1975) 259–273.
[27] A. Winfree, The Geometry of Biological Time, second ed., Springer Verlag, New York, 2001.
[28] G.B. Ermentrout, D.H. Terman, Mathematical Foundations of Neuroscience, Vol. 35, Springer, New York, 2010.
[29] Y. Kuramoto, Chemical Oscillations, Waves, and Turbulence, Springer-Verlag, Berlin, 1984.
[30] B. Pietras, A. Daffertshofer, Network dynamics of coupled oscillators and phase reduction techniques, Phys. Rep. (2019).
[31] B. Monga, D. Wilson, T. Matchen, J. Moehlis, Phase reduction and phase-based optimal control for biological systems: a tutorial, Biol. Cybernet. 113 (1–2) (2019) 11–46.
[32] D. Jordan, P. Smith, Nonlinear Ordinary Differential Equations: An Introduction for Scientists and Engineers, Vol. 10, Oxford University Press, Oxford, 2007.
[33] D. Wilson, J. Moehlis, Isostable reduction of periodic orbits, Phys. Rev. E 94 (5) (2016) 052213.
[34] D. Wilson, Phase-amplitude reduction far beyond the weakly perturbed paradigm, Phys. Rev. E 101 (2) (2020) 022220.
[35] D. Wilson, Optimal control of oscillation timing and entrainment using large magnitude inputs: An adaptive phase-amplitude-coordinate-based approach, SIAM J. Appl. Dyn. Syst. 20 (4) (2021) 1814–1843.
[36] D. Wilson, Isostable reduction of oscillators with piecewise smooth dynamics and complex Floquet multipliers, Phys. Rev. E 99 (2) (2019) 022210.
[37] J.P. Hespanha, Linear Systems Theory, Princeton University Press, Princeton, New Jersey, 2018.
[38] G. Dumont, B. Gutkin, Macroscopic phase resetting-curves determine oscillatory coherence and signal transfer in inter-coupled neural circuits, PLoS Comput. Biol. 15 (5) (2019) e1007019.
[39] E. Montbrió, D. Pazó, A. Roxin, Macroscopic description for networks of spiking neurons, Phys. Rev. X 5 (2) (2015) 021028.
[40] H. Schmidt, D. Avitabile, E. Montbrió, A. Roxin, Network mechanisms underlying the role of oscillations in cognitive tasks, PLoS Comput. Biol. 14 (9) (2018) e1006430.
[41] C. Bick, M. Goodfellow, C.R. Laing, E.A. Martens, Understanding the dynamics of biological and neural oscillator networks through exact mean-field reductions: a review, J. Math. Neurosci. 10 (2020) 1–43.
[42] T.W. Ko, G.B. Ermentrout, Phase-response curves of coupled oscillators, Phys. Rev. E 79 (1) (2009) 016211.
[43] Z. Levnajić, A. Pikovsky, Phase resetting of collective rhythm in ensembles of oscillators, Phys. Rev. E 82 (5) (2010) 056202.
[44] Y. Kawamura, H. Nakao, K. Arai, H. Kori, Y. Kuramoto, Collective phase sensitivity, Phys. Rev. Lett. 101 (2) (2008) 024101.
[45] K. Toth, D. Wilson, Control of coupled neural oscillations using near-periodic inputs, Chaos 32 (3) (2022).
[46] J. Rubin, D. Terman, High frequency stimulation of the subthalamic nucleus eliminates pathological thalamic rhythmicity in a computational model, J. Comput. Neurosci. 16 (2004) 211–235.
[47] E. Ott, C. Grebogi, J.A. Yorke, Controlling chaos, Phys. Rev. Lett. 64 (11) (1990) 1196.
[48] K. Pyragas, Continuous control of chaos by self-controlling feedback, Phys. Lett. A 170 (6) (1992) 421–428.
[49] W.L. Ditto, S.N. Rauseo, M.L. Spano, Experimental control of chaos, Phys. Rev. Lett. 65 (26) (1990) 3211.
[50] Y. Wang, F.M. Li, Y.Z. Wang, Homoclinic behaviors and chaotic motions of double layered viscoelastic nanoplates based on nonlocal theory and extended Melnikov method, Chaos 25 (6) (2015).
[51] E. Brown, J. Moehlis, P. Holmes, On the phase reduction and response dynamics of neural oscillator populations, Neural Comput. 16 (4) (2004) 673–715.
[52] J.L. Proctor, S.L. Brunton, J.N. Kutz, Dynamic mode decomposition with control, SIAM J. Appl. Dyn. Syst. 15 (1) (2016) 142–161.
[53] S.L. Brunton, J.N. Kutz, Data-Driven Science and Engineering: Machine Learning, Dynamical Systems, and Control, Cambridge University Press, New York, 2019.